Malaysian Journal of Catalysis
http://mjcat.utm.my/
MJCat
Research Article

Effect of Ni/Al-MCM-41 Impregnation Method on Catalytic Deoxygenation of Reutealis Trisperma Oil

Reva Edra Nugraha[1]*, Rida Kharismawati[2], Suprapto Suprapto[2], Abdul Aziz[3], Holilah Holilah[4,5], Hartati Hartati[6], Didik Prasetyoko[2*]

[1]*Department of Chemical Engineering, Faculty of Engineering, Universitas Pembangunan Nasional "Veteran" Jawa Timur, Surabaya, East Java, 60294, Indonesia*
[2]*Department of Chemistry, Faculty of Science and Data Analytics, Institut Teknologi Sepuluh Nopember, Keputih, Sukolilo, Surabaya, 60111, Indonesia*
[3]*Department of Pharmacy, Kader Bangsa University, Palembang, South Sumatera, 30253, Indonesia*
[4]*Research Center for Biomass and Bioproducts, National Research and Innovation Agency of Indonesia (BRIN), Cibinong, 16911, Indonesia*
[5]*Department of Food Science and Technology, Faculty of Agriculture, Halu Oleo University, Indonesia*
[6]*Department of Chemistry, Faculty of Science and Technology, Universitas Airlangga, Surabaya, 60115, Indonesia*

**Corresponding Author: reva.edra.tk@upnjatim.ac.id; didikp@chem.its.ac.id*

Article history:
Received 11 June 2023
Accepted 01 August 2023

ABSTRACT

Deoxygenation of Reutealis trisperma oil into green diesel has been carried out using Ni/Al-MCM-41 catalyst. The Ni/Al-MCM-41 catalyst was prepared using the wetness impregnation and incipient wetness impregnation methods, hereinafter referred to as Ni/Al-MCM-41 (WI) and Ni/Al-MCM-41 (IWI). XRD and FTIR analysis shows a characteristic of the amorphous phase for solid Al-MCM-41 catalyst. FTIR pyridine was used to assess the impact of the NiO impregnation technique on Lewis acid and Brønsted acidity. The acidity test showed that the Ni/Al-MCM-41 (WI) catalyst had the highest total acidity 0.227 mmol/g. The catalytic activity of Ni/Al-MCM-41 catalyst was examined in the deoxygenation reaction of Reutealis trisperma oil under inert conditions for 4 hours. In comparison to Ni/Al-MCM-41(IWI) and Al-MCM-41 catalysts, the Ni/Al-MCM-41(WI) catalyst produced better results in the deoxygenation reaction of Reutealis trisperma oil. Impregnation with WI method gives higher Lewis acidity which results in increasing RTO conversion via the deoxygenation reaction pathway and suppresses the cracking reaction. Consequently, intensify the green diesel (C11-18) hydrocarbon products with selectivity of 100% and a degree of deoxygenation of 92.77%.

Keywords: *Deoxygenation, Al-MCM-41, Impregnation, Hydrocarbon*

| eISSN 0128-2581 |

1. INTRODUCTION

The development of renewable alternative energy was getting immersive attentions due to the depletion of fossil fuels [1]. An alternative fuel called biodiesel is typically produced by transesterification and esterification processes between oil and alcohol in the presence of catalyst. A number of biodiesel's downsides include poor storage stability, less steady flow properties in cold conditions, limited oxidation stability, and a low cetane value [2]. Fatty acids can be transformed into more stable straight-chain alkanes, such as green diesel, to overcome the biodiesel weakness. The advantages green diesel includes the production of oxygen-free hydrocarbons (high oxidation stability), complete combustion, high energy density, low by-product production and improved performance in cold temperatures [3].

The raw material often used in the production of green diesel is vegetable oil i.e., jatropha oil [4], waste cooking oil [5], ceiba oil, sterculia oil [6], microalgae [7], fallopian japonica oil [8] etc. Sources of non-food vegetable oils (non-edible oil) such as Reutealis trisperma oil are found in many regions of Indonesia. Reutealis trisperma oil is regarded as a viable raw material because of its high oil content (38–40%) and excellent productivity (3.8–7.7 tons/ha/year) [9]. Vegetable oil can be converted into green diesel fuel via catalytic cracking, hydrotreating, and deoxygenation [10,11]. Deoxygenation reactions provide several advantages over hydroprocessing processes for the vegetable oils conversion including high yield production, faster reactions and majority fraction produced is a hydrocarbon group [4].

Zeolites like H-ZSM-5 [12], Y-zeolite [13] and H-β [14] as well as mesoporous materials like MCM-41 [15]and

SBA-15 [16] are a few types of catalysts that can be used in deoxygenation reactions. Mesoporous Al-MCM-41 increased the conversion of Jatropha curcas oil to long-chain (C_{11}-C_{18}) green diesel hydrocarbons, as we have previously reported [17,18]. The strong acidity has an advantage because it speeds up the isomerization reaction and improves the fuel's quality.

In many different catalytic reactions, impregnation of transition metal has been extensively used. Metal oxides can have an impact on the catalytic efficacy and stability of the catalyst, resulting in enhanced conversion, selectivity, and reaction yield [19]. Ni metal oxide is widely used in catalysts due to its less expensive and more plentiful than precious metals [16]. The synthesis of Al-MCM-41 material impregnated in two distinct ways was performed in this study to test its effect on the deoxygenation reaction of Reutealis trisperma oil.

2. EXPERIMENTS

2.1 Synthesis of Al-MCM-41

The hydrothermal approach was utilized to synthesis Al-MCM-41 with the mole ratio of $10Na_2O$: $100SiO_2$: $2Al_2O_3$: $1800H_2O$. The synthesis of Al-MCM-41 in this study utilized kaolin as a source of silicate (SiO_2) and aluminate (Al_2O_3). NaOH was dissolved with distilled water and stirred for 30 minutes. Kaolin is added to the NaOH solution with faster stirring. Add LUDOX and distilled water gently while swirling vigorously after creating the sol. At room temperature for eight hours, the sol mixture was agitated to homogeneity. The product was subsequently put through a six-hour at 70 °C for aging process. The first hydrothermal process was then carried out at 80 °C for 12 hours, and the crystallization process was then stopped by cooling the mixture with running water. The CTAB was added gradually with continuously stirring. At 150 °C for 24 hours, the second hydrothermal procedure was conducted. The hydrothermal gel that resulted was neutralized with distilled water to a pH of 7, then dried for 24 hours at 60 °C in the oven. The dry solid is then calcined at 550 °C (2 °C/min) for 1 hour with N_2 gas flow and followed by 6 hours with air flow.

2.2 Synthesis of Ni/Al-MCM-41

Catalyst Al-MCM-41 was used as support and nickel as impregnated metal with the content of 10%. In this study, the efficacy of two impregnation methods; wet impregnation and incipient wetness impregnation was evaluated.

The first impregnation method was carried out by the wet impregnation method which adapted from Baharudin et. al., (2019) [16]. Firstly, a 10 mL solution of a 1:1 ethanol-water ratio was used to dissolve 0.49 grams of Ni $(NO_3)_2.6H_2O$. After being thoroughly blended, 0.9 gram of Al-MCM-41 was added and swirled for three hours at room temperature. The solution is then gradually heated to 80 °C with continuously stirring and a pale green suspension remained. After that, it was dried for 24 hours at 80 °C in the oven and calcined at 550 °C (2 °C/min) for 1 hour with N_2 gas followed by air flow for for 6 hours with air flow. The wet-impregnated sample is referred to as Ni/Al-MCM-41 (WI).

The incipient wetness impregnation procedure was carried out by dissolving 0.49 grams of Ni $(NO_3)_2.6H_2O$ in 1 mL of a 1:1 ethanol-water solution until homogenous. The nickel nitrate solution was then added dropwise while stirring into 0.9 grams of Al-MCM-41. The nickel nitrate is applied until the entire supporting surface is soaked. Stirring was done for 2 hours, followed by drying in an oven at 80°C for 24 hours. The dry solid was then calcined at 550°C (2°C/min) under N_2 gas flow for 1 hour, followed by air flow for 6 hours. The wet impregnated sample is referred to as Ni/Al-MCM-41 (IWI).

2.3 Catalyst Characterization

X-ray Diffraction (XRD) characterization utilizing a PHILIPS-binary XPert with MPD diffractometer with Cu K radiation operating at 30 mA and 40 kV was used to examine the phase transformation of kaolin to aluminosilicate structure and Ni deposition on catalyst support. Shimadzu Instrument Spectrum One 8400S's Fourier Transform Infra-Red (FTIR) within range of 400-1400 cm^{-1} measurement was used to examine the functional group of catalyst. FTIR Spectroscopy was also used to determine Brønsted and Lewis acid sites in Ni/Al-MCM-41 and Al-MCM-41.

2.3 Catalytic Activity

A 100 mL-3 neck flask with a simple distillation apparatus and a heating mantle was used for the deoxygenation reaction of Reutealis trisperma oil. Prior to the reaction, 0.3 gram of catalyst was added to 10 grams of Reutealis trisperma oil and flowed with N_2 gas to create an inert atmosphere for the reaction. The mixture was then heated to 350 °C with continuously stirring and N_2 was flowing for 4 hours. The yield and conversion of the reaction can be determined from the reaction's results using Equations (1) and (2).

$$Liquid\ yield\ (\%) = \left(\frac{weight\ of\ liquid\ product}{weight\ of\ reactant}\right) x100\% \quad \text{Eq. 1}$$

$$Conversion\ (\%) = \left(\frac{weight\ of\ initial\ reactant - weight\ of\ final\ reactant}{weight\ of\ initial\ reactant}\right) x100\% \quad \text{Eq. 2}$$

The liquid deoxygenated product was then examined with GC-MS (Gas Chromatography-Mass Spectrometry). Equations (3) and (4) can be used to calculate the degree of deoxygenation and product selectivity.

$$Degree\ of\ deoxygenation = \left[1 - \left(\frac{\%FA\ in\ liquid\ product}{\%FA\ in\ reactant}\right)\right] x100\% \quad \text{Eq. 3}$$

$$Selectivity = \frac{(peak\ area\ of\ desired\ hydrocarbon)}{(peak\ area\ of\ total\ hydrocarbon)}\ x\ 100\% \quad \text{Eq.4}$$

3. RESULTS AND DISCUSSION

3.1 XRD Analysis

In this study, XRD analysis was performed with the range of 2θ=5- 50° for Al-MCM-41 and 2θ=5-80° for Ni/Al-MCM-41. The diffraction pattern of Al-MCM-41 and Ni/Al-MCM-41 were shown in Figure 1 dan Figure 2. The characteristic peak of the Al-MCM-41 material may be seen in the diffractogram of the material at 2θ=15–30°. This peak suggests the presence of an amorphous phase in the Al-MCM-41 material [20,21]. The impregnated Ni on Al-MCM-41 catalyst exhibits additional peaks at 2θ= 37°, 43°, 62°, and 75° which are associated with the diffraction planes (111), (210) (220), and (311) of face-centered cubic NiO [22,23]. The presence of the characteristic NiO peak shows that NiO was impregnated successfully on the surface of Al-MCM-41 [4].

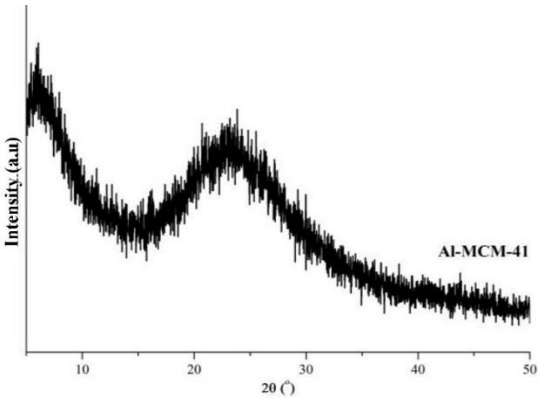

Figure 1. Diffraction pattern of Al-MCM-41

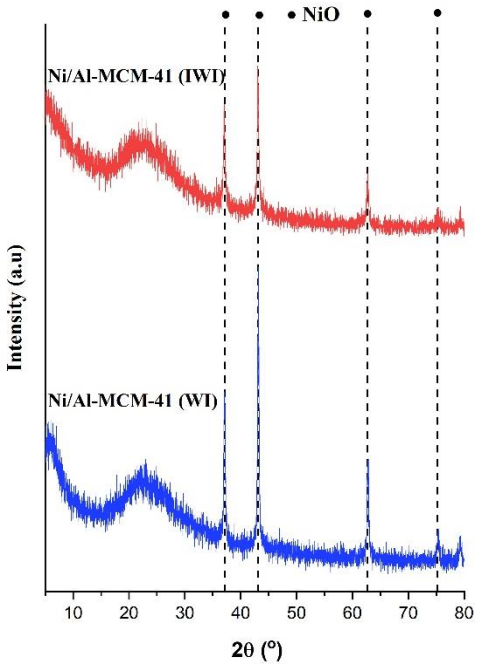

Figure 2. Diffraction pattern of Ni/Al-MCM-41

Table 1 displays the NiO crystallite sizes for both Ni/Al-MCM-41 catalysts which were determined using the Debye Scherrer equation at 2θ=37° (111). In contrast to Ni/Al-MCM-41(IWI), NiO particles are smaller in the Ni/Al-MCM-41(WI) catalyst. The variation in crystal size reveals the impregnation technique affected nickel dispersion in the Al-MCM-41 catalyst.

Table 1. Crystallite size NiO with Debye Scherrer equation

Catalyst	2θ (°)	FWHM (rad)	B (°)	d (nm)
Ni/Al-MCM-41 (IWI)	37.0558	0.1004	0.001752	83.4
Ni/Al-MCM-41 (WI)	37.0661	0.1506	0.002628	55.5

3.2 FTIR Analysis

The FTIR spectra of Al-MCM-41 was shown in Figure 3. Five distinctive absorption peaks were detected from Al-MCM-41 catalyst. The asymmetric stretching of Si–O–Si bands was appeared in absorption band of 1234 cm^{-1} [22,24]. The peak at 470 cm^{-1} is due to the T-O bond's bending vibrations, where T is an atom of Si or Al. Si-O-Si vibration exhibits an internal asymmetric stretching vibration at wave number 1100 cm^{-1}, while Si-O-Al bonds are present at wave number 799 cm^{-1}. A mesoporous structure characteristic is shown by the peak at wave number 968 cm^{-1}, which is caused by the vibration of silanol groups (Si-OH).

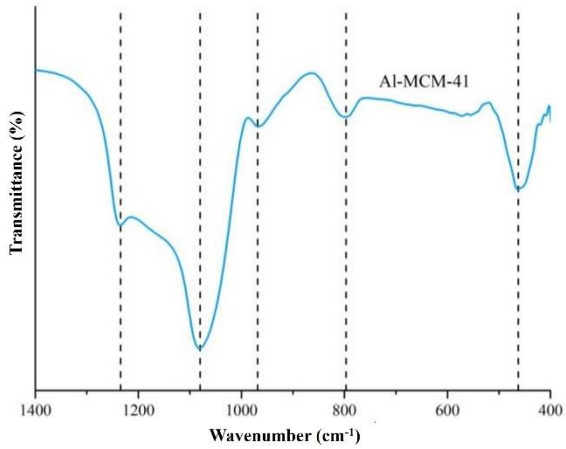

Figure 3. FTIR spectra of Al-MCM-41

3.3 Catalyst Acidity

The pyridine adsorption FTIR was used to determine the number and kind of acid sites on the catalyst. The pyridine-FTIR spectra of all samples show three adsorption peaks at 1446, 1490 and 1546 cm^{-1} which correlated to Lewis and Brønsted acid sites [25,26]. The adsorption peak at 1446 cm^{-1} was generated due to the transferring electron

pairs from the secondary amine group in pyridine to Lewis acid sites in the catalyst. Meanwhile, adsorption at 1546 cm^{-1} correspond to proton transfer from Brønsted acid sites to form a pyridinium ion ($C_5H_5NH^+$) with a pyridine molecule [27]. The adsorption peak at wave number 1490 cm^{-1} associated to the total peak of both Lewis acid and Brønsted acid sites.

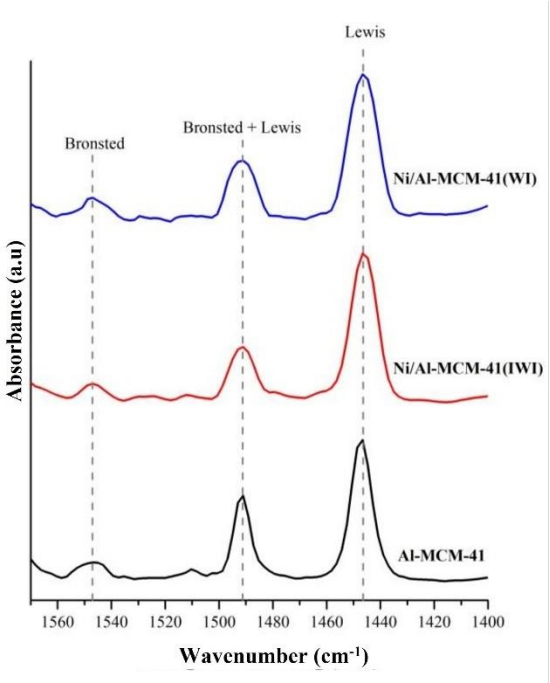

Figure 4. Pyridine-FTIR spectra of Al-MCM-41 and Ni/Al-MCM-41

The number of acid Al-MCM-41 and Ni/Al-MCM-41 catalysts was summarized in Table 2. The acidity of the Lewis acid sites increases with a trend of Ni/Al-MCM-41(WI)>Ni/Al-MCM-41(IWI)>Al-MCM-41. This implies an effect of NiO addition to the quantity of Lewis acid. The inclusion of NiO, on the other hand, reduces the amount of Brønsted acid sites. The decrease in Brønsted acid on the Ni/Al-MCM-41 catalyst was caused by proton exchange of Ni^{2+} ions from NiO from Si-O-Al framework [16].

Table 2. Number of Brønsted and Lewis acid sites of catalysts

Catalysts	Acid Sites (mmol/g)		Lewis+ Brønsted (mmol/g)
	Lewis	Brønsted	
Al-MCM-41	0.154	0.042	0.196
Ni/Al-MCM-41 (IWI)	0.168	0.028	0.197
Ni/Al-MCM-41 (WI)	0.196	0.031	0.227

3.4 Catalytic Activity

The catalytic activity was tested in the deoxygenation reaction of Reutealis trisperma oil. The deoxygenation reaction was carried out for 4 hours at 350 °C with a N_2 gas flow. In this catalytic activity test, the GC-MS instrument was utilized to perform qualitative and quantitative analysis on the deoxygenation process product. The conversion, yield and degree of deoxygenation of liquid product obtained from different catalysts was shown in Table 3. The Lewis acid sites of the Ni/Al-MCM-41 (WI) catalyst is greater than Ni/Al-MCM-41 (IWI) and Al-MCM-41 catalysts, resulting in higher conversion and yield. Increasing the Lewis acid sites can boost catalytic activity in the Reutealis trisperma oil deoxygenation reaction which correlated to the C–C bond breaking that occurs on the Lewis acid sites [17].

Table 3. Conversion, yield and degree of deoxygenation of liquid product

Catalysts	Conversion (%)	Yield (%)	Degree of Deoxygenation
Al-MCM-41	36.4	11.8	89.38
Ni/Al-MCM-41 (IWI)	49.0	16.1	91.10
Ni/Al-MCM-41 (WI)	55.4	20.1	92.77

Figure 5 depicts the distribution of hydrocarbon molecules resulting from the deoxygenation reaction. The deoxygenation reaction produces short chain hydrocarbons (C_{9-10}) and long chain hydrocarbons (C_{11-18}). The deoxygenation reaction using the Ni/Al-MCM-41(WI) catalyst generated a selectivity of hydrocarbon compounds (C_{11-18}) of 100%, with C_{15} and C_{17} hydrocarbons composition of 92.77%. The liquid product obtained by using Ni/Al-MCM-41 (IWI) catalyst produces selectivity of 95.33% for hydrocarbon compounds (C_{11-18}) and 4.67% for hydrocarbons (C_{9-10}) in with a major product selectivity of 81.01% for C_{15} and C_{17} hydrocarbons. The hydrocarbon selectivity (C_{9-10}) of Al-MCM-41 was 12.13%, and the hydrocarbon selectivity (C_{11-18}) was 87.87%.

All catalysts exhibit a dominant yield of C_{15} and C_{17} hydrocarbon chains which could raise the cetane number (CN) value as an indicator of fuel quality for ignition [28]. This suggests that the predominant reaction pathway in this reaction is the decarboxylation pathway. The decarboxylation route will result in straight chain alkanes with one less carbon atom than the original fatty acids and CO_2 gas as a by-product since Reutealis trisperma oil contains palmitic acid (C16:0), oleic acid (C18:1), and linoleic acid (C18:2) [17]. Therefore, a renewable, sustainable, and alternative biofuel, known as green diesel, is absolutely necessary to replace petroleum-based diesel and biodiesel in terms of effluent, no pollution, and economic attractiveness/cheapness, with the consumption of green diesel projected to increase to 3% annually in the upcoming 2030. Even the green diesel is regarded as the greenest, most economical, and potentially useful fuel to be utilized in diesel engines and produced on an industrial scale in the recent and future to minimize environmental pollution and to satisfy the rising diesel fuel demand [19].

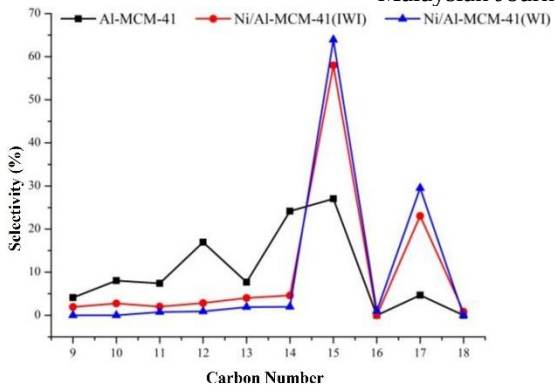

Figure 5. Hydrocarbon distribution from catalytic deoxygenation reaction of Reutealis trisperma oil

4. CONCLUSION

In this study, Al-MCM-41 and Ni/Al-MCM-41 has been successfully synthesized. All the catalysts show amorphous phase structure of MCM-41 and additional peak of NiO particle on Ni/Al-MCM-41. The NiO particle size on the Ni/Al-MCM-41 (WI) and NiAl-MCM-41 (IWI) catalysts were 55.5 nm and 83.4 nm. The Ni/Al-MCM-41 (WI) catalyst have the highest acid site with composition of Lewis acid of 0,196 mmol/g and Brønsted acid of 0.031 mmol/g. The Ni/Al-MCM-41 (WI) catalyst exhibited the highest hydrocarbon selectivity of 54.24% which was corroborated by the catalyst's high degree of deoxygenation in comparison to the Al-MCM-41 and Ni/Al-MCM-41 catalysts (IWI).

ACKNOWLEDGEMENTS

The authors acknowledge the Ministry of Research, Technology and Higher Education of Republic Indonesia under PDUPT research grant with contract number 1489/PKS/ITS/2022 and Universitas Pembangunan Nasional “Veteran” Jawa Timur under Riset Dasar scheme with contract number of SPP/108/UN.63. B/LT/V/2023 for funding the research.

REFERENCES

1. P. Balakrishnan, M.S. Shabbir, A.F. Siddiqi, X. Wang, Energy Sources, **42** (2020) 2698–2703.
2. N. Hongloi, P. Prapainainar, C. Prapainainar, Review of green diesel production from fatty acid deoxygenation over Ni-based catalysts, Molecular Catalysis **523** (2021) 111696.
3. R. Sotelo-boyás, F. Trejo-zárraga, F. de J. Hernández-Loyo, Hydrogenation, IntechOpen, 2012: 187–216.
4. N. Asikin-Mijan, H. V Lee, G. Abdulkareem-alsultan, A. Afandi, Journal of Cleaner Production **167** (2017) 1048–1059.
5. G.A. Alsultan, N. Asikin-Mijan, H. V. Lee, A.S. Albazzaz, Y.H. Taufiq-Yap, Energy Conversion Management, **151** (2017) 311–323.
6. N. Asikin-Mijan, H. V. Lee, J.C. Juan, A.R. Noorsaadah, H.C. Ong, S.M. Razali, Y.H. Taufiq-Yap, Applied Catalysis A: General **552** (2018) 38–48.
7. N.A.A. Rahman, J. Fermoso, A. Sanna, Fuel Processing Technology **173** (2018) 253–261.
8. W. Bambang, G. Guan, J. Rizkiana, X. Du, X. Hao, Z. Zhang, A. Abudula, Bioresources Technology **179** (2015) 518–523.
9. M.Y. Abduh, Syaripudin, L.W. Putri, R. Manurung, Energy Reports. **5** (2019) 1375–1380.
10. R.W. Gosselink, S.A.W. Hollak, S.W. Chang, J. Van Haveren, K.P. De Jong, J.H. Bitter, D.S. Van Es, ChemSusChem. **6** (2013) 1576–1594.
11. K.W. Jeon, H.S. Na, Y.L. Lee, S.Y. Ahn, K.J. Kim, J.O. Shim, W.J. Jang, D.W. Jeong, I.W. Nah, H.S. Roh, Fuel **258** (2019) 116179.
12. A. Veses, B. Puértolas, J.M. López, M.S. Callén, B. Solsona, T. García, ACS Sustainable Chemistry & Engineering, **4** (2016) 1653–1660.
13. M. Choo, L.E. Oi, T.C. Ling, E. Ng, Y. Lin, G. Centi, J.C. Juan, Journal of Analytical and Applied Pyrolysis, **`47** (2020) 104797.
14. F.P. Sousa, L.N. Silva, D.B. de Rezende, L.C.A. de Oliveira, V.M.D. Pasa, Fuel **223** (2018) 149–156.
15. K. de Sousa Castro, L. Fernando de Medeiros Costa, V.J. Fernandes, R. de Oliveira Lima, A. Mabel de Morais Araújo, M.C. Sousa de Sant’Anna, N. Albuquerque dos Santos, A.D. Gondim, RSC Advances **11** (2021) 555–564.
16. K.B. Baharudin, Y.H. Taufiq-Yap, J. Hunns, M. Isaacs, K. Wilson, D. Derawi, Microporous Mesoporous Materials, **276** (2019) 13–22.
17. R.E. Nugraha, D. Prasetyoko, H. Bahruji, S. Suprapto, N. Asikin-Mijan, T.P. Oetami, A.A. Jalil, D.-V.N. Vo, T.-Y. Yun Hin, RSC Advances, **11** (2021) 21885–21896..
18. R.E. Nugraha, D. Prasetyoko, N. Asikin-Mijan, H. Bahruji, S. Suprapto, Y.H. Taufiq-Yap, A.A. Jalil, Microporous Mesoporous Materials, **315** (2021) 110917.
19. H.I. Mahdi, A. Bazargan, G. McKay, N.I.W. Azelee, L. Meili, Chemical Engineering Research and Design, **174** (2021) 158–187.
20. F. Guo, J. Li, W. Li, X. Chen, H. Qi, X. Wang, Y. Yu, Quinoline Russian Journal of Applied Chemistry, **90** (2017) 2055–2063.
21. C. Huo, J. Ouyang, H. Yang, Scientific Reports, **4** (2015).
22. J. Xu, P. Xia, F. Guo, J. Xie, Y. Xia, H. Tian, Internationa Journal of Hydrogen Energy, **45** (2020) 30484–30495.
23. S. Qiu, X. Zhang, Q. Liu, T. Wang, Q. Zhang, L. Ma, Catalysis Communication, **42** (2013) 73–78.
24. F. Sahel, F. Sebih, S. Bellahouel, A. Bengueddach, R. Hamacha, Research on Chemical Intermediates, **46** (2020) 133–148.

25. S. Bailleul, I. Yarulina, A.E.J. Hoffman, A. Dokania, E. Abou-Hamad, A.D. Chowdhury, G. Pieters, J. Hajek, K. De Wispelaere, M. Waroquier, J. Gascon, V. Van Speybroeck, Journal of the American Chemical Society, **141** (2019) 14823–14842.
26. X. Li, D. Han, H. Wang, G. Liu, B. Wang, Z. Li, J. Wu, Fuel. **144** (2015) 9–14.
27. H. Li, Y. Wang, F. Meng, H. Chen, C. Sun, S. Wang, RSC Advances, **6** (2016) 99129–99138.
28. S.K. Bhatia, R. Gurav, T.R. Choi, H.R. Jung, S.Y. Yang, H.S. Song, Y.G. Kim, J.J. Yoon, Y.H. Yang, Energy Conversion Management, **192** (2019) 385–395.

Malaysian Journal of Catalysis
http://mjcat.utm.my/
MJCat
Research Article

Extraction and Characterization of Keratin Protein from Chicken Feathers using Alkaline Hydrolysis Method: Effects of Sodium Sulphide Concentration and Shelf-life Evaluation

Z. Aliyu[1], A. D. Mahmud[1,] *, A. B. Oluwatoyin[1], A. Aliyu[1], A. S. Yahaya[1], A. M. Saleh[1]

[1] *Department of Chemical Engineering, Ahmadu Bello University, Zaria, Nigeria.*

**Corresponding Author: admahmud@abu.edu.ng*

Article history:
Received 4 November 2023
Accepted 24 December 2023

ABSTRACT

This study investigated the extraction of keratin protein from chicken feathers through alkaline hydrolysis using sodium sulphide as a digesting agent. The protein was precipitated using hydrogen chloride and confirmed through biuret test, solubility test, sulphur test, and FT-IR analysis. The effect of varying sodium sulphide concentrations (0.5M, 0.75M, and 1M) on the extracted keratin was evaluated. Results showed that a higher concentration of sodium sulphide produced a higher yield of keratin, with 1M producing 65.8% yield. However, the shelf-life of wet keratin extracted using 1M concentration was four weeks, compared to six weeks for 0.5M and 0.75M concentrations. The dried keratin was unaffected after six weeks. The study suggests that a higher concentration of the reducing agent produced a higher yield of keratin protein but with a shorter shelf-life if drying was not carried out. The utilization of abundant waste generated by poultry industries is crucial in reducing pollution and creating opportunities for valuable product development. The extraction of keratin from chicken feathers provides an eco-friendly approach to waste management and creates opportunities for product development.

Keywords: *Keratin, Chicken feathers, Shelf-life, Yield, Drying, Hydrolysis*

| eISSN 0128-2581 |

1. INTRODUCTION

Keratin is a vital and abundant structural protein in humans and animals, which can be found in various industrial wastes such as slaughterhouse by-products, skin remains, animal hair, horns, hooves, and feathers [1-4]. These wastes are considered environmental pollutants due to their resistance to physical, chemical, and biological agents [5]. Keratin has a complex hierarchical structure that can be classified into primary, secondary, and tertiary structures. It also occurs abundantly in two forms which are α-keratins and β-keratins, with the former occurring in mammals and the latter in birds and reptiles [6], [7]. This work focuses on the extraction of keratin from chicken feathers, which have received significant attention in various applications, such as cosmetics, tissue engineering, and regenerative medicine, due to their biocompatibility, biological function, and biodegradability [8].

Chicken feathers are a rich source of keratin, with a large quantity being produced as a by-product of the poultry industry each year [9], [10]. Its primary structure consists of a repeating pattern of four amino acids: glycine, alanine, serine, and tyrosine. This pattern is repeated many times to form a long polypeptide chain. This unique sequence of amino acids gives chicken feather keratin its unique properties, including its strength, flexibility, and resilience. However, conventional methods of extracting keratin, such as acidic hydrolysis, can cause damage to some amino acids and consume a large quantity of reagents, which cannot be recycled [11]. Therefore, alternative methods, such as enzymatic hydrolysis and chemical-enzymatic treatment, have been proposed to produce hydrolyzed keratin protein [12]. Ionic liquids (ILs) have also been studied for their potential to dissolve biopolymers, including keratin, into useful materials for industrial applications [1].

The secondary structure of chicken feather keratin is characterized by alpha-helices, which are formed when the polypeptide chain twists around itself. The alpha-helices then associate with one another to form coiled-coil structures, which in turn associate to form protofilaments. The protofilaments then bundle together to form intermediate filaments, which are the structural components of keratin fibers. The tertiary structure of keratin involves the folding and packing of the intermediate filaments into a

three-dimensional structure. This three-dimensional structure gives keratin its unique properties and allows it to form strong and resilient fibers [13].

Alkaline extraction using sodium sulphide has been shown to be an efficient and economically favorable method that preserves the secondary structure of the protein, while the addition of an ionic surfactant such as sodium dodecyl sulphate can prevent the aggregation of keratin polypeptide chains [9]. Enzymatic catalysis hydrolysis is a promising alternative method, but its industrial application is hindered by the outer protective film and compact structure of the feather [12]. Therefore, developing effective and eco-friendly processes to extract keratin from poultry feathers is desirable from both environmental and economic perspectives [9].

2. MATERIALS AND METHODS

The use of chemical (alkaline) hydrolysis was employed in the extraction process with sodium sulphide as the reducing agent. The extraction method was carried out by different stages of experimental procedures as listed below and all the chemicals used were of analytical grade requiring no further purification.

2.1 Collection and pretreatment of waste chicken feathers

Chicken feathers were collected from Samaru market, latitude 11.1617 ˚N and longitude 7.6479 ˚E. The feathers were washed with distilled water to remove all the accompanied blood and dirt. It was then soaked in detergent for 2 hours, and washed with distilled water, after which it was oven dried at 60 ˚C for 12 hours. The dried feathers were soaked in diethyl ether for 12 hours to cleanse it from stain, oil and grease, then washed with hot water (100 ˚C) followed by distilled water and then oven dried at 60 ˚C for 48 hours to remove its moisture content. The dried chicken feathers were ground using a laboratory milling machine at mesh size 0.25 mm and stored in a sealed plastic bag at room temperature.

2.2 Keratin protein extraction

1 L of 0.5 M sodium sulphide solution was prepared in a 2000 mL beaker. 25 g of the ground chicken feathers was weighed and added to the sodium sulphide solution. The solution was heated to the temperature of 60 ˚C at a pH of 10 and stirred continuously for 6 hours using a magnetic stirrer. The solution was centrifuged at 10,000 rpm for 10 minutes. The supernatant liquid was carefully collected then filtered using the burchner funnel with filter paper of 110 mm to make it particle free.

2.3 Protein precipitation

After the extraction process, the pH of the keratin solution was adjusted to 3.5 by addition of HCl to precipitate the protein. The solution was then centrifuged at 10,000 rpm for 6 minutes and the solid particles carefully collected.

2.4 Protein purification

400 mL distilled water was added to the keratin protein collected and stirred (washing). The solution was centrifuged at 10,000 rpm for 6 minutes and the solid particles collected carefully for further analysis and characterization.

The above steps were repeated for sulphide concentration 0.75 M and 1 M.

2.5 Analysis and characterization of the keratin protein

2.5.1 General test (Biuret test)

5% sodium hydroxide solution and 1% copper sulphate solution were prepared. 2 mL of each keratin solution (0.5 M, 0.75 M, 1M) was mixed with the sodium hydroxide solution in the ratio 1:1. Three drops of the copper sulphate solution were added to the mixture solutions. Changes in the solution were observed and recorded.

2.5.2 Differentiating test (Solubility test)

10 mL of distilled water was added to each keratin protein in a test tube. The test tubes were then shaken vigorously for a minute and observations recorded.

2.5.3 Confirmatory test (Sulphur test)

40% sodium hydroxide solution and 2% lead acetate solution were prepared. 2 mL of each keratin protein was mixed with the sodium hydroxide solution in the ratio 1:1. The solution in the test tubes were held on flame and boiled for 1 minute, then cooled under tap. 5 drops of the lead acetate solution were added to the mixture solution and changes observed and recorded.

2.5.4 Fourier Transform Infrared Spectroscopy

Functional groups of the extracted protein were investigated by mixing samples into KBr pellets using Fourier transform infrared (FT-IR) absorption spectrum Agilent spectrometer (30 scans with 8 cm^{-1} resolution) in the wavenumber range of 650–4,000 cm^{-1}.

2.5.5 Shelf-Life

A sample of the wet keratin extracted was segregated and kept in a sealed container, while some part was shadow dried for 72 hours at room temperature, crushed into fine powder and kept in another sealed container. Both samples were then observed for 6 weeks.

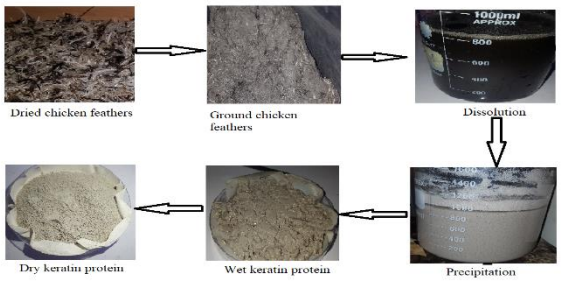

Figure 1. Schematic diagram of the keratin extraction process

3. RESULTS AND DISCUSSION

3.1 Extraction of Keratin from Chicken Feathers

Alkaline hydrolysis was carried out to extract keratin from chicken feathers using 0.5M, 0.75M and 1M concentration of the reducing agent, sodium sulphide (Na2S). Table 1 shows the physical observation, moisture content, yield and shelf-life after extraction.

Table 1. Physical appearance of extracted keratin

Concentration (M)	0.5	0.75	1
% Moisture Content (MC)	70	74.5	78.1
% Protein Yield	55.7	61.6	65.8
Shelf-life (weeks)	4	6	6
Physical Appearance	Most compacted	Moderately compacted	Least compacted with a smoother appearance

The wet keratin (keratin before drying) extracted for the 1 M concentration appeared to be smoother and loose indicating high amount of water present. While the 0.5 M concentration was the least loose, showing low amount of water. The solubility of the feathers is dependent on the concentration of Na^2S, temperature and process time [14].

As seen in Table 1, the concentration of the reducing agent affects the appearance, associated water as well as the yield of the extracted protein. The amount of keratin yield in the final product depends on the degree of hydrolysis of the feather. Hence, the 1 M concentration shows the highest degree of hydrolysis. This contradicts the work of Gindaba et al. [15] which says that at 0.5 M the yield decreases on increasing concentration of the solvent. The increasing pattern of keratin yield is caused by peptide and disulphide bonds cleavage. The effect of concentration of sodium sulphide at constant temperature and pH is shown in Figure 2.

The samples of wet and dried keratin proteins were observed for 6 weeks under atmospheric conditions. At week 4, the 1 M wet keratin was observed to have some microbial growth while the 0.5 M, 0.75 M and all the dried keratins appeared the same. At week 6, there was some microbial growth on the 0.5 M and 0.75 M wet keratin and none for the dry keratins of all concentration. The onset of the contamination for the 1 M keratin was due to the high amount of moisture present providing the environment for the growth.

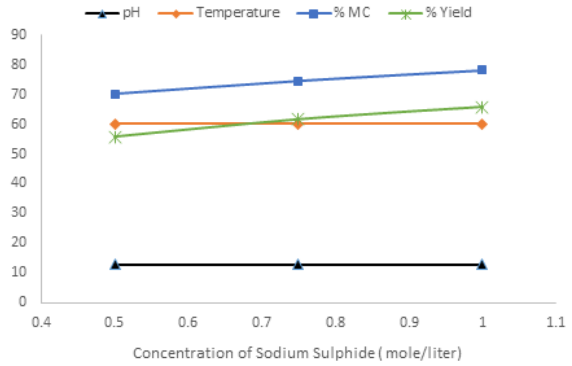

Figure 2. Effect of concentration of sodium sulphide at constant temperature and pH

3.2 Characterization of the Extracted Protein

3.2.1 Biuret test

The protein solution remained its usual colour (ash) on the addition of the NaOH solution. It turned purple however on the addition of the copper sulphate solution indicating the presence of peptide linkage as shown in Figure 3. This is a general test for all types of protein where the Cu^{2+} ions react with the nitrogen of the peptide bond to form a purple colour complex.

Figure 3. Biuret test for extracted protein from chicken feather

3.1 Extraction of Keratin from Chicken Feathers

Alkaline hydrolysis was carried out to extract keratin from chicken feathers using 0.5 M, 0.75 M and 1 M.

3.2.2 Solubility test

On addition of water, the keratin was observed to be insoluble as shown in Figure 4. This is due to the presence of the disulphide bonds present making it insoluble. It differentiates it from the rest of the proteins that are highly soluble owing to the hydrophilic amino acids present in them.

Figure 4. Solubility test for extracted protein from chicken feather

3.2.3 Sulphur test

The protein solution turned black on the addition of the lead acetate shown in Figure 5, confirming the presence of cysteine which is a major component of keratin. Upon boiling of the keratin solution with sodium hydroxide, the sulphur present in its amino acids i.e., cysteine is converted to inorganic sodium sulphide. It then reacts with lead to form lead sulphide that forms black coloured pigments inside the solution.

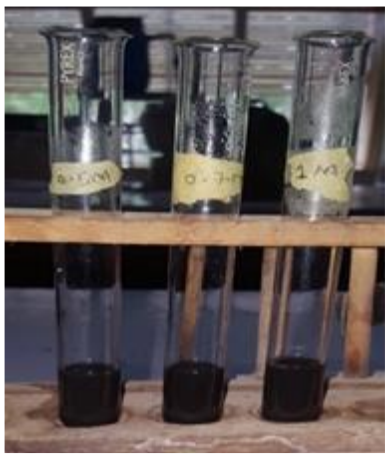

Figure 5. Confirmatory test for extracted protein from chicken feather

3.3 Fourier Transform Infrared (FT-IR)

Keratin is a natural polymer with a complicated structure, hence the need for Fourier Transform of Infrared (FTIR) to understand all details of structure of keratin. The characteristic bands and signals from these spectra were analysed in order to confirm the products as keratin. Figure 6-9 shows the characteristic absorption bands for the keratin extracted.

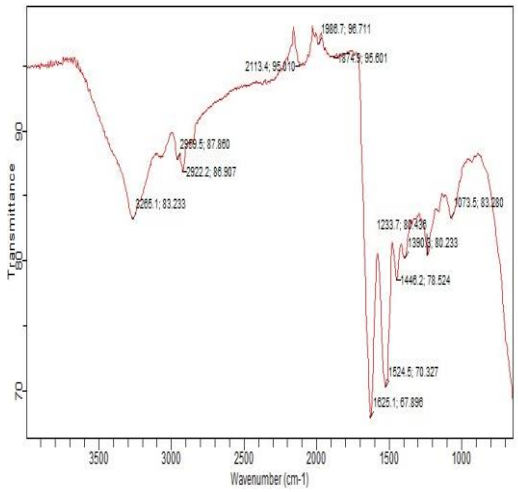

Figure 6. FT-IR of chicken feathers

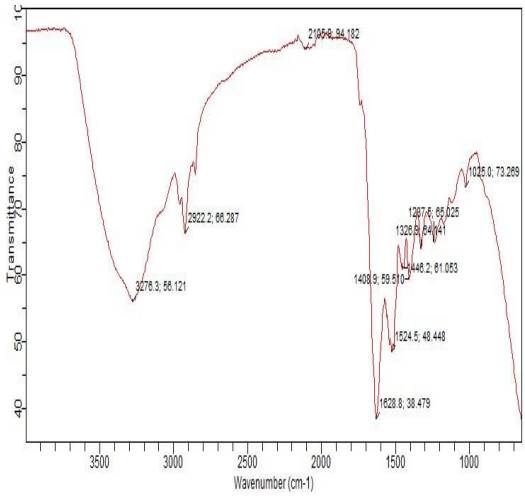

Figure 7. FT-IR of Extracted Protein of 0.5 M

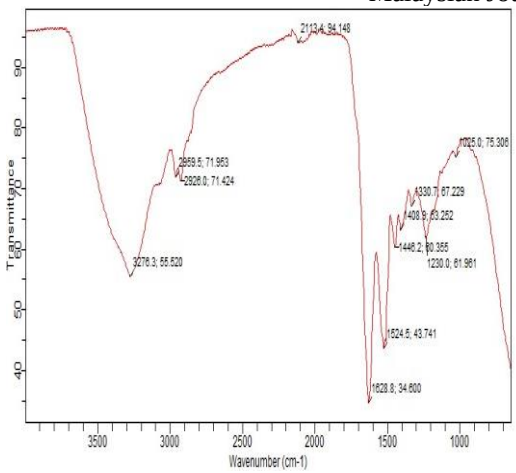

Figure 8. FT-IR of Extracted Protein of 0.75 M

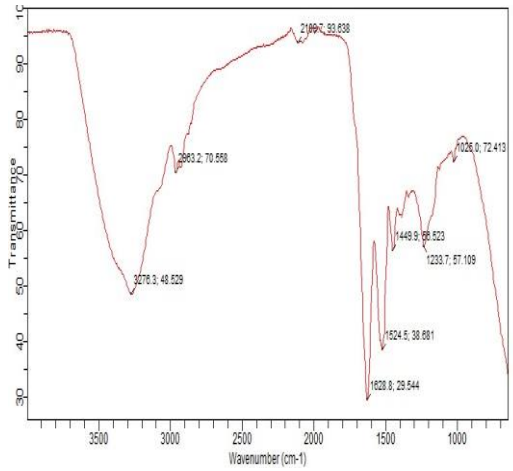

Figure 9. FT-IR of extracted protein of 1M

4. CONCLUSION

Sodium sulphide proved to be a highly effective dissolution agent, while hydrogen chloride demonstrated excellent precipitating properties. Notably, at a concentration of 1M alkalis, the extracted keratin exhibited a loose appearance, with a moisture content of 78.2%, a yield of 65.8%, and a shelf-life of only 4 weeks. These findings suggest that higher concentrations of the dissolution agent led to greater keratin extraction. Furthermore, this extraction process is suitable for scaling up from the laboratory to the industrial level.

ACKNOWLEDGEMENTS

The research team will like to acknowledge Ahmadu Bello University Zaria and Petroleum Technology Development Funds for providing research laboratories.

REFERENCES

1. Idris, A., Vijayaraghavan, R., Rana, U. A., Fredericks, D., Patti, A. F., & MacFarlane, D. R. **12** (2012) 207890.
2. Kalia, S. Springer Nature Switzerland AG (2019).
3. Reddy, N. (2017).
4. Teresa, K., & Justyna, B. Waste Management, **31** (2011) 1689-1701.
5. Kumawat, T. K., Sharma, A., Sharma, V., & Chandra, S. Keratin (2015).
6. Barone, J. K., Schmidt, W. F., Gregoire, N. T. Journal of Applied Polymer Science, **100** (2005) 1432–1442.
7. Kamarudin, N. B., Sharma, S., Gupta, A., Kee, C. G., Chik, S. M., & Gupta, R.. 3 Biotech **7** (2017).
8. Agarwal, V., Panicker, A. G., Indrakumar, S., & Chatterjee, K. International Journal of Biological Macromolecules, **133** (2019) 382-390.
9. Ji, Y., Chen, J., Lv, J., Li, Z., Xing, L., & Ding, S. Separation and Purification Technology **132** (2014) 577-583.
10. Olonilebi, J. O. Journal of Food and Quality Control, **3** (2017) 1-8.
11. Wang, Y., & Cao, X. (2012). Process Biochemistry, **47**(5) (2012) 896–899.
12. Alahyaribeik, S., & Ullah, A. International Journal of Biological Macromolecules, **148** (2020) 449-456.
13. De Guzman, R. C., & Tomalia, D. A. In Advances in Clinical Chemistry, **55** (2011) 75–96.
14. Abebe, T. Extraction and Optimization of Natural Protein (Keratin) from Waste Chicken Feather for the Development of Anti-Ageing Cream (2017).
15. Gindaba, G. T., Filate, S. G., & Etana, B. B. International Journal of Modern Science and Technology, **4**(7) (2019) 174–179.

Malaysian Journal of Catalysis
http://mjcat.utm.my/
MJCat Research Article

Experimental Study of The Pressure Drop Rotating and Flooding in A Packed Bed Reactor

Usman Garba[1,2*] David Rouzineau[1,] Michel Meyer[1]

[1]*Chemical Engineering Laboratory, University of Toulouse, CNRS, INPT, UPS, Toulouse, France*
[2]*Usmanu Danfodiyo University Sokoto, Nigeria*

**Corresponding Author: usman.garba@udusok.edu.ng*

Article history:
Received 01 November 2023
Accepted 11 December 2023

ABSTRACT

The almost zero sensitivity to variations in gravitational force offered by rotating packed bed (RPB) reactors as gas/liquid contactor for multi-phase catalytic reactions was explored. A pilot-scale RPB with a casing diameter of 0.676m, inner rotor diameter of 0.160m, and an outer rotor diameter of 0.500m equipped with a standard, multi-layered, stainless steel wire mesh packing of axial height 0.040m, a specific surface of 2400 m^2/m^3 and a porosity of 86% was used. The scarcity of fundamental data on the hydrodynamics and mass transfer of the reactor limits the design, scale-up, and retrofitting of RPB reactors. Hence, the focus was on the hydrodynamic behaviour of the device. Previous studies on RPB reactor flooding and operating limits dwelled on visual observations and pressure drop variations only. However, physical visualizations are subjective because pressure drop variations of RPB reactors are too inconsistent to be used in obtaining the upper operating limit during their operations. A robust quantitative method of obtaining RPB reactor flooding limits based on the flow rate of the ejected liquid, supported by visual observation and pressure drop measurement, was presented for a rotation speed range, gas flowrate and, liquid flowrate range of 0 -1500 rpm, 0 - 400 Nm^3h^{-1} and 0-0.84 m^3h^{-1} respectively. The aim was to identify, with greater certainty, RPB reactor hydrodynamic characteristics and provide a more standard method of identifying it. The average increase in single-phase pressure drops per unit increase in rotation speed and the average increase in pressure drop per unit increase in gas flow rate was 0.75Pa/rpm and 4.11Pa/m^3h^{-1} respectively. The upper operating limits found showed that to attain a particular capacity of RPB reactors at a given gas and liquid flowrates, a particular rotation speed is required which can simply be altered to vary the other operating parameters towards attaining stable operations.

Keywords: *Rotating packed bed reactor, Pressure drop, Flooding, Gas-liquid contactor, heterogeneous catalytic reactions*

| eISSN 0128-2581 |

1. INTRODUCTION

Reliance on gravitational force makes conventional packed columns for separation processes such as distillation and absorption have unimpressive sizes and physical footprints which makes them uneconomical, especially where space and weight are limited[1], [2]. The operating ranges of non-rotating, conventional, packed bed columns (PBCs) are limited by gravitational and frictional forces acting in opposite directions on the down-flowing liquid and the gas flowing from the bottom of the column. A RPB reactor, also called HIGEE (High g) contactor, is a compact process intensification equipment in which a combination of sizeable allowable gas and liquid flow rates is achieved by superimposing gravitational force with centrifugal force. In RPB reactors, the higher gravitational force factor employable raises the combined operating range of the throughputs in addition to their flexibility due to the additional degree of freedom offered by the rotation speed [3].

A fundamental aspect of the modelling, design, optimization, and implementation of pilot-scale and subsequent scale-up of RPB reactors is the clear understanding of the principles of its hydrodynamics via accurate prediction of the pressure drops and upper operating limits [3], [4]. Also, Zhang et al. [6] observed that the mass transfer performance and efficiency of an RPB reactor, as reflected by its gas pressure drop, is closely linked to its hydrodynamic characteristics, operating costs, and energy requirements. Hydrodynamic characteristics such as

the pressure drop of an RPB reactor are a useful index in measuring its resistance and consequent energy consumption [7]. Many studies were carried out to evaluate the influence of pressure drop in many RPB reactor operations with empirical and semi-empirical models established [8], [9]. RPB reactor hydrodynamic parameters extensively reported in the literature include liquid holdup [10], [11], gas pressure drop (Neumann et al., 2017b; Pyka et al., 2022), liquid dispersion [11], [14] and, flooding [4], [15]. Although extensive research has been conducted and documented using RPB reactors, with many of its applications explored at the industrial scale, its design approach is still case-specific. It thus requires improvements (Neumann, et al., 2017a).

Cortes et al. [17] reviewed various advantages and disadvantages of RPB reactors regarding its mass-transfer performance, hydrodynamic behaviour, as well as the complexity and suitability of the rotor to be filled with catalyst packing for the purpose of heterogeneous reactions. The relatively high rotation speeds of RPB reactors combined with the size of the equipment make it possible to implement forces more than 100 times greater than gravity, greatly intensifying the transfer phenomena between phases [18]. Rapid contact surface replacement in RPB reactors allows for high effective surface area packings of 2000 to 5000m^2/m^3 [18]. This allows for higher mass transfer characteristics: gas-liquid interfacial area, gas-side and liquid-side volumetric mass transfer coefficients, and height of transfer unit (Cheng & Tan, 2011; Zhang et al., 2011). Also, this allows for the same separation performance in RPB reactor to have much more flexible and compact equipment with a wider operating range than a gravity column used for absorption [19]. Overall, compared to conventional gravity columns, for a comparable processing capacity and efficiency, a RPB reactor offers rotation as an extra degree of freedom, serves as the foundation of modular plants, and is more miniaturized with higher flexibility and energy efficiency [21]. The characteristics mentioned above make RPB reactors emblematic equipment for process intensification. Consequently, RPB reactors have been employed for various purposes in diverse fields such as separation processes, synthesis, and preparation of micro and nano-particles, petroleum products processing, biodiesel production, medical sciences, and pollution control [2], [19], [21].

Results of preliminarily studies involving liquid–solid processes conducted by [22], [23] and [24] revealed that the apparent reaction rates of heterogeneous catalytic reactions can be increased 33–39 times when conducted in RPB reactor reactors compared to when conducted in conventional packed bed reactors. In their study, Chang et al. [22], used RPB reactor as a catalytic ozonation reactor for the decomposition of phenol and reported that the process efficiency was influenced by the rotation speed, catalyst packing mass, UV irradiation intensity, ozone gas flow rate and temperature. The modelling of the integration of simultaneous reaction and stripping for an esterification reaction was achieved in a solid catalyzed reactive RPB stripper was reported by Gudena et al. [23]. At a rotation speed of at 1000 rpm, the results, showed a 56% enhancement in concentration of produced octyl-hexanoate ester and a 30% rise in ester concentration when the RPB stripper was used as compared to when traditional reactors are used. Also, the dissolution of copper by potassium dichromate to study the liquid–solid mass transfer in a RPB reactor equipped with a structured foam packing was use to lay the foundation for the modelling of RPB reactors for heterogeneous catalytic reaction by Liu et al. [25]. The liquid–solid volumetric mass transfer coefficient was found to be in the range 0.04–0.14 s^{-1}, and was about 500% higher than what was obtained with a conventional packed bed reactor. The findings above as reported in [21] - [24] attests to the potentials of the RPB reactor for multi-phase catalytic reactions. However, Liu et al. [25] observed that the paucity of the fundamental understanding and data on the complex liquid–solid mass transfer in RPB reactors is a limitation to its design and scale-up. Hence, the need for more fundamental studies on the RPB reactor.

A sketch of a conventional, single-stage RPB reactor as presented by Garba et al. [26] is shown in Figure 1. It comprises of a casing surrounding a rotor mounted on a shaft and rotated by a motor. The rotor is a motor-driven, ring-shaped cylinder that encloses an annular packing mounted on either a horizontal or a vertical shaft. In countercurrent operation mode, gas is introduced into the outer periphery of the packing from the casing. The liquid is usually introduced into the center (or “eye”) of the rotor via the liquid inlet through a stationary set of nozzles (liquid distributor) into the packing from the top of the RPB. After its transformation by centrifugal shear forces, the liquid flows in the form of rivulets, droplets, or films as determined by the rotation speed [10]. The casing wall finally collects it and flows downwards under gravity, leaving the casing via the liquid outlet.

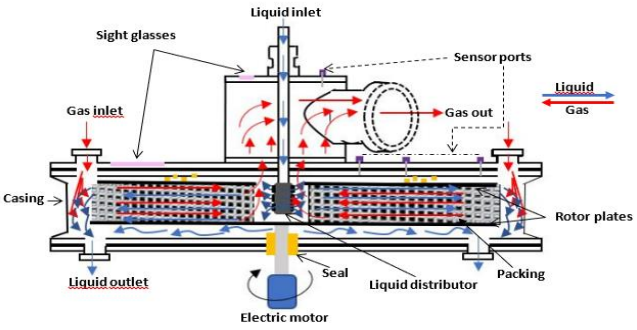

Figure 1. Schematic of a countercurrent flow RPB reactor [26]

As equipment for efficient multi-phase mixing and mass transfer, [27] identified RPB packing as its core component. Because of its excellent mass transfer characteristics, stainless steel wire mesh is commonly used as RPB packing [28]. For catalyzed reactions, in addition to the ease in catalysts loading, the high centrifugal force field

in RPB reactors, has necessitated the use of structured as opposed to pellet catalysts to prevent squeezing and possible crushing of the catalysts. Also, the use of structured catalysts packing can overcome the cumbersome step of bulk catalysts loading [24].

Conventional separation packed beds have constant cross-sections. Thus, their packing pores are nearly wholly filled throughout the column during flooding, causing a noticeable, steep rise in pressure drop. However, due to the rotor geometry, RPB reactor packings have variable cross-sections. The centrifugal forces are lowest at the center (eye) of the rotor. Hence, RPB reactor flooding occurs in the eye from where the liquid is ejected. Consequently, pressure drop variations during flooding in RPB reactors are not consistent as the sole indicator of flooding. (Neumann et al., 2017a), and Lockett [15] also reported that in contrast to conventional columns, for RPB reactors, no sharp inflection in the total pressure drop or the holdup of the liquid with the gas velocity was observed during flooding. The procedure for visually determining the upper operating limit is to neutralize two operating variables and manipulate the third one [3]. Therefore, it is possible to carry out two procedures to reconfirm the results. The speed of the rotor and the liquid flow rate may be set to a constant value then the gas flow rate gradually increases until an excessive splash of the liquid is observed in the eye of the rotor. Allowing the gas flow rate to increase beyond the upper operating limit will cause the liquid to accumulate in the eye of the rotor. (Groß et al., 2018; Neumann et al., 2017b) recommended the use of a combination of visual and quantitative approaches to adequately study the flow behavior in RPB reactors, while [3] observed that due to observed inconsistencies, the use of physical and visual observations and the measurement of pressure drop variations alone are not sufficiently adequate to predict flooding behavior in RPB reactors. [10] used liquid holdup, while [4] measured the flow rate of entrained liquid from the eye of the rotor to identify the upper operating limits in RPB reactors.

This work presents a robust quantitative method of obtaining RPB reactor upper operating limit based on the flow rate of the ejected liquid, supported by visual observation and pressure drop measurements. This was achieved by connecting a hydrocyclone to the gas outlet. In addition, a comprehensive pressure drop behavior and flooding for a countercurrent water-air system and a single-block stainless steel wire mesh packing using a double jet nozzle for the liquid inlet were used to study the hydrodynamics of the pilot-scale RPB reactor. The aim was to improve further the understanding of RPB reactor hydrodynamics for design, scale-up, and energy conservation purposes.

2. EXPERIMENTS

The experimental setup is shown in Figure 2. The RPB reactor was a commercial pilot-scale RPB reactor 500 supplied by ProCeller®, Poland. The RPB reactor was a single-stage, vertical rotor type with a casing diameter of 0.676m, an inner rotor diameter of 0.160m, and an outer rotor diameter of 0.500m. The packing was supplied along with the RPB reactor reactor and it was a conventional, multi-layered, single-block, stainless steel wire mesh with an axial height of 0.040m, a specific surface of 2400 m^2/m^3, and a porosity of 86%. Visual observation was possible using two inspection glasses placed directly above the eye of the rotor and another on the casing (Figure 3a). To aid the systematic collection and subsequent measurement of ejected water from the eye of the rotor during flooding, a hydrocyclone was connected to the gas outlet. A countercurrent air-water system was used for all the experiments. The rotation speed of the rotor was selected and auto-controlled via a variable frequency drive. The liquid was pumped to the RPB reactor using a peristaltic pump and controlled with a valve.

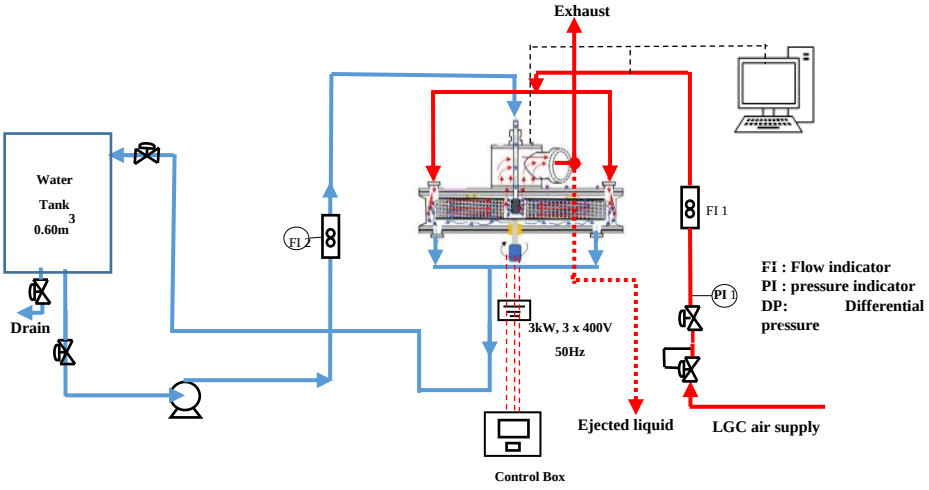

Figure 2. Countercurrent process flow diagram of the RPB reactor

The liquid flow rate was measured with a panel-type rotameter and sprayed from the center of the RPB reactor using a dual nozzle, flat fan liquid distributor. The liquid was recirculated to the feed tank using a bypass line. An air supply from the general laboratory compressor was used. The gas was introduced into the outside of the RPB reactor into the casing through twin gas inlets and leaves after passing through the packing via the gas outlet. While the liquid sprays outwards from the center of the packing to its periphery. A pressure sensor connected to a pressure transmitter was placed across the two points to measure the pressure drop between the packing periphery and the gas outlet. Pressure drop was measured in real time by interfacing the sensor to a computer using a data acquisition system.

The range of operating parameters studied was: gas flow rate (V_G), 0-400Nm^3/h; liquid flow rate (V_L), 0-0.84m^3/h and rotation speed 0-1500 revolutions per minute (RPM). Each experimental run was for 5 minutes. In the dry pressure drop measurements, the frictional pressure drop was first measured by passing air at 100Nm^3/h through the stationary rotor and then measuring the pressure drop. The experiment was repeated by increasing the airflow rate in steps of 50Nm^3/h. The same procedure was repeated with the rotor at various rotation speeds. Next, the effect of the rotation speed was investigated, initially via the centrifugal pressure drop. Without liquid and gas flow, the rotor was set to an initial speed of 100 rpm. The rotation speed was subsequently changed stepwise. The effect of rotation speed was further investigated by varying the rotation speed at constant gas flow rates. For the wet pressure drop, rotation speeds and liquid flow rates were kept while the gas flow rate was increased stepwise. This was followed by another set of experiments during which the gas flow rate and rotation speed were kept constant while the liquid flow rate was increased. The liquid flow rate and rotation speed were kept constant to determine the upper operating limit. In contrast, the gas flow rate was increased stepwise until the first drops of water were observed from the gas outlet according to the arrangement shown in Figure 3e. This point was taken as the upper operating limit of the RPB reactor at the prevailing combination of operating factors. The reduction in rotation speed was continued gradually, with the amount of ejected water measured at each step after attaining a steady state of operation. Flooding points of the RPB reactor operations were determined by visual observation of excessive water splashing at the RPB reactor eye, with or without a sharp increase in pressure drop. The volume of water ejected at each step change of the gas flowrate was collected and measured using a measuring cylinder, and the flooding point was taken following the recommendation of [4] when the flow rate of the ejected liquid is the same or exceeds 8 % of the liquid flow rate.

3. RESULTS AND DISCUSSION

3.1 Effect of operating parameters on the single-phase pressure drops

Figure 3 shows the influence of the gas flow rate and the rotation speed on the single phase (dry) pressure drop. Figure 3 (a) shows the dry pressure drop increases with increase in rotation speed. A slow increase in the pressure drop was obtained at low rotational speeds from 100 to 550 rpm. Above 600 rpm, a rapid and almost linear increase in pressure drop was obtained. This phenomenon may be due to the greater need to overcome the pressure drop caused by rotation (centrifugal head) at higher rotational speeds, which consequently causes the air in the rotor and between it and the casing to rotate. The dry bed average increase in pressure drops per unit increase in rotation speed in the range investigated was 0.75Pa/rpm. This shows that centrifugal pressure contributes significantly to the total dry-packing pressure drop. Figure 3(b) shows a substantially linear increase in pressure drop with increasing gas flow rate. The effects of gas inertia and friction primarily cause this. On average, Figure 3(b) shows that the average increase in pressure drop per unit increase in gas flow rate was 4.11Pa/Nm^3h^{-1} within the operating range investigated.

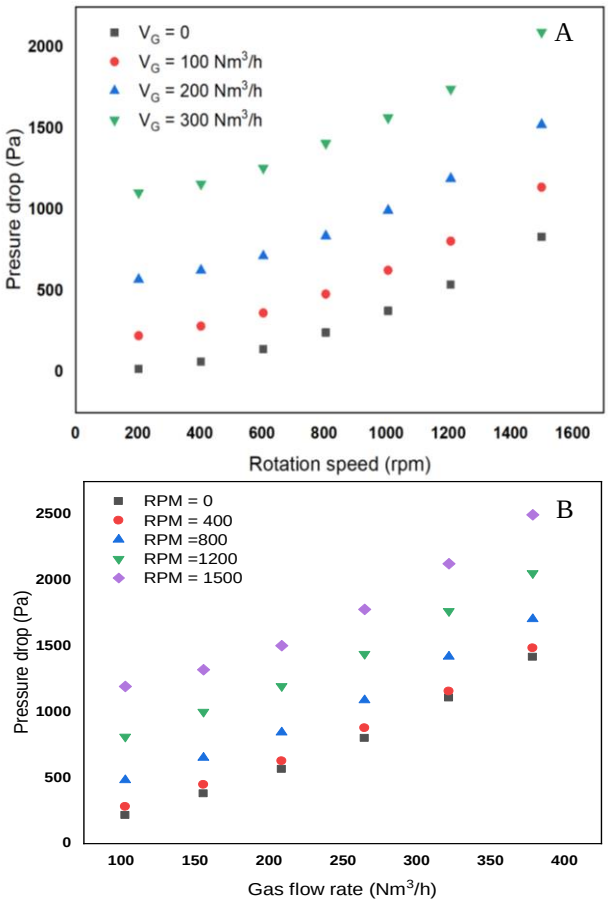

Figure 3. Dry bed pressure drops (A) effect of rotation speed (B) effect of gas flowrate

3.2 Effect of operating parameters on the total pressure drop

For the irrigated bed, Figures 4(a) and (b), shows that the trend of the pressure drop variation was similar to that of the dry bed, with the pressure drop increasing with an increase in rotational speed and with the gas flow. [5] identified the wetting of the packing surface, which affects the frictional pressure drop, and the blockage of the packing pores by the liquid to the passage of gas as the two principal contributors to the rise in pressure drop in wet RPB reactors.

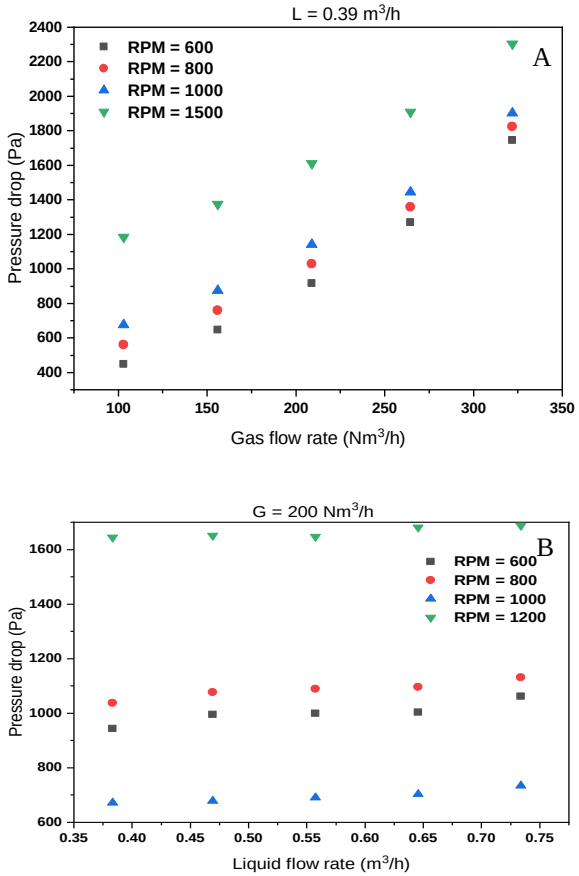

Figure 4. Wet bed pressure drops (A) effect of gas flowrate (B) effect of liquid flowrate

Figure 4(b) indicates the lower effect of liquid flow rate on the overall pressure drop in RPB reactors. For example, for a gas flow of 350Nm^3/h, the 50% increase in liquid flow rate from 0.3 to 0.6 m^3/h produces small changes in the pressure drop with the increase in the speed of rotation, showing that the effect of the gas flow in the RPB reactor is more than that of the liquid flows. The average unit increase of 5.73Pa/Nm^3/h for a fixed liquid flow rate of 0.39 m^3/h indicates the higher pressure drop due to the presence of the liquid as opposed to the 4.11 Pa/Nm^3/h. This phenomenon is more visible when we represent this at constant rotational speeds with a variation of the gas flow (Figure 4a) or a variation of the liquid flow (Figure 4(b). These results confirm the trends described by the reports of [3], [16]. Additionally, in terms of liquid loading loads and gas capacities, it can be deduced that the ranges of the wet pressure drops in Figures 5(a) and (b) are comparable to the findings of [7].

3.3 The upper operating limit of the RPB reactor

Figure 5 (a) shows that the flooding data follows a typical RPB reactor equipped with a vertical axis pressure drop variation curve with rotation speed at constant gas and liquid flow rates, as highlighted by [16]. A lowering of centrifugal pressure drop is obtained at a decrease from the maximum rotation speeds. At the same time, liquid accumulation in the eye causes only slight increases in frictional pressure drop. Further decrease in the rotation speed will cause an accumulation of liquid in the eye of the rotor, which leads to an increase in the frictional pressure drop and a sharp increase in the total pressure drop.

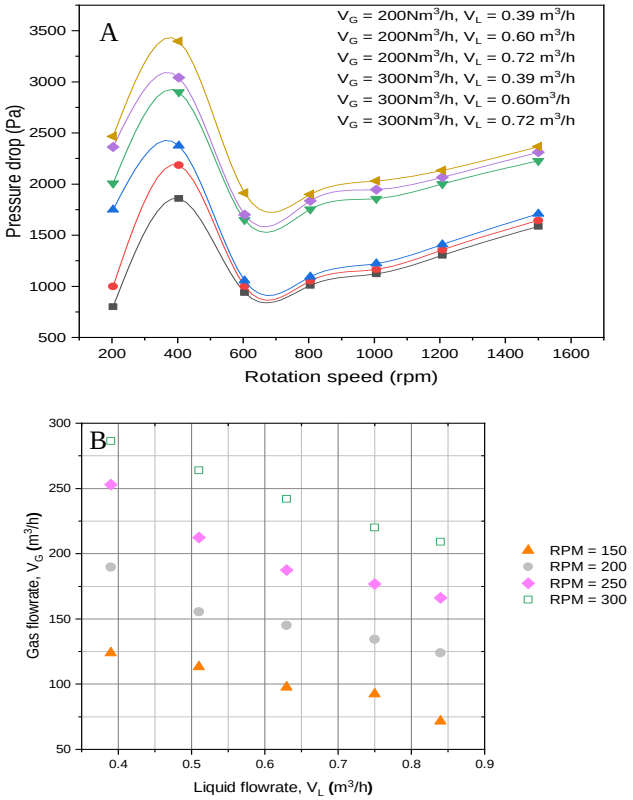

Figure 5. (A) Effect of rotation speed at constant gas and liquid flow rates (B) upper operating points

As the rotation speed is further decreased, rapid ejection of liquid from the eye of the rotor to the gas outlet is obtained due to the acceleration of the liquid droplets. The pressure drop increases significantly, and the presence of water is visually observable in the rotor eye. Figure 5(b) shows the upper operating limits of the system investigated. At a constant rotation speed, the gas flow rate at which the ejection of liquid droplets was observed and decreased with an increased liquid flow rate. Regular operation of the RPB reactor without liquid ejection and possible high-pressure drops, which increase power consumption, is obtained by operating the RPB reactor below the indicated points. The

operating limit at a given condition can be improved by increasing the rotation speed from the given point. Based on a range of liquid loads and the gas capacity factor at the inner radius of the RPB reactor, the trends and ranges of these operating limits are comparable to the results of [3].

4. CONCLUSION

This paper focused on furthering the understanding of the fundamentals of the RPB reactor as an intensified reactor for enhancing heterogeneous catalytic reactions. The barrier imposed by the lack of fundamental data on the design modelling and scale-up of RPB reactor reactors was bridged by the presenting hydrodynamic characteristic data necessary for the evaluation of the mass transfer processes. Hence, the gas pressure drops of a pilot-scale RPB reactor equipped with stainless steel wire mesh packing for an air-water system using a twin-nozzle liquid distributor was explored. A robust approach to determine RPB reactor operating limits based on quantifying the volume of liquid ejected from the eye of the rotor was explored. Low rotational speeds from 100 to 550 RPM generate slow increase in pressure drop while rotation speeds above 600 rpm generated rapid and almost linear increase in pressure drop. The trends were attributed to the higher need to overcome the centrifugal head caused by rotation at higher rotational speeds which forces the rotation of the gas entrapped in the reactor. Within the range of operating conditions investigated, the average increase in pressure drop per unit increase in rotation speed was 0.75Pa/rpm. The operating limits for RPB reactor are influenced mainly by the three operational parameters: gas flow rate, liquid flow rate, and rotational speed in that order.

ACKNOWLEDGEMENTS

This work was conducted under support funding from the Overseas Scholarship Scheme (OSS) of the Petroleum Technology Development Fund (PTDF), Nigeria (Grant Number: PTDF/ED/OSS/PHD/UG/1543/19).

REFERENCES

1. Adekola Lawal, O. O., Meihong, W., Peter, S., Fuel, **101** (2012) 115–128.
2. Hilpert, M., and Repke, J. U., Ind. Eng. Chem. Res, **60** (2021) 5251–5263. doi: 10.1021/acs.iecr.1c00440.
3. Groß, K., Neumann, K., Skiborowski, M., and Górak, A., Chem. Eng. Trans. **69** (2018) 661–666. doi: 10.3303/CET1869111.
4. Hendry, J. R., Lee, J. G. M., and Attidekou, P. S., Chem. Eng. Process. - Process Intensif. **151** (2020) 107908. doi: 10.1016/j.cep.2020.107908.
5. Zhang, W., Xie, P., Li, Y.L., Teng, and Zhu, J., J. Nat. Gas Sci. Eng. **79** (2020) 103373. doi: 10.1016/j.jngse.2020.103373.
6. Wen, Z. N., Wu, W., Luo, Y.,. Zhang, L. L., Sun, B. C., and Chu, G. W., Ind. Eng. Chem. Res. **59** (2020) 16043–16051. doi: 10.1021/acs.iecr.0c01886.
7. Liu, X., Jing, M., Chen, S., and Du, L., Can. J. Chem. Eng. **96** (2018) 90–596. doi: 10.1002/cjce.22936.
8. Singh, S. P. et al., Ind. Eng. Chem. Res. **31** (1992) 574–580. doi: 10.1021/ie00002a019.
9. Jiao, W. Z., Liu, Y. Z., and Qi, G. S., Ind. Eng. Chem. Res. **49** (2010) 3732–3740. doi: 10.1021/ie9009777.
10. Burns, J. R., Jamil, J. N., and Ramshaw, C., Chem. Eng. Sci. **55** (2000) 2401–2415. doi: 10.1016/S0009-2509(99)00520-5.
11. Burns, J. R. and Ramshaw, C., Chem. Eng. Sci. **51** (1996) 1347–1352. doi: 10.1016/0009-2509(95)00367-3.
12. Pyka, T. J., Koop, C. Held, and G. Schembecker, Ind. Eng. Chem. Res. (2022). doi: 10.1021/acs.iecr.2c02500.
13. Neumann, K., Hunold, S., Skiborowski, M., and Górak, A., Ind. Eng. Chem. Res. **56** (2017) 12395–12405. doi: 10.1021/acs.iecr.7b03203.
14. Xie, P. (2019).
15. Lockett, M. J., Chem. Eng. Res. Des. **73** (1995) 379–384.
16. Neumann, K., Hunold, S., Groß, K., and Górak, A., Chem. Eng. Process. Process Intensif., **121** (2017) 240–247. doi: 10.1016/j.cep.2017.09.003.
17. Cortes Garcia, G. E., van der Schaaf, J., and Kiss, A. A. J. Chem. Technol. Biotechnol. 92 (2017) 1136–1156. doi: 10.1002/jctb.5206.
18. Pan, S. Y., Wang, P., Chen, Q., Jiang, W. Y. H., and Chiang, P. C., J. Clean. Prod. 149 (2017) 540–556. doi: 10.1016/j.jclepro.2017.02.108.
19. Zhang, L. L., Wang, J. X., Xiang, Y., Zeng, X. F., and Chen, J. F., Ind. Eng. Chem. Res. 50 (2011) 6957–6964. doi: 10.1021/ie1025979.
20. Cheng, H. H., and Tan, C. S., Sep. Purif. Technol. **82** (2011) 156–166. doi: 10.1016/j.seppur.2011.09.004.
21. Neumann, K., et al., Chem. Eng. Res. Des. **134** (2018) 443–462. doi: 10.1016/j.cherd.2018.04.024.
22. Chang, C., Chiu, C., Chang, C., and Chang, C., J Hazmat. **168** (2009) 49–55. doi: 10.1016/j.jhazmat.2009.02.171.
23. Gudena Krishna, G. P. R., Tay Haw Min, Chem. Eng. Sci. **80** (2012) 242-252.
24. Liu, Y., Li, Z., Chu, G., Shao, L., Luo, Y., and Chen, J., Chinese J. Chem. Eng. **28** (2020) 2507–2512. doi: 10.1016/j.cjche.2020.06.038.
25. Ya-zhao Liu, J. C., Li, Z., Chu, G., Shao, L., Luo. Y., Chinese J. Chem Eng. **28** (2020) 2507–2512.
26. Garba, U., Rouzineau, D., and Meyer, M., MATEC Web Conf. **04003** (2023) 1–8, [Online]. Available: https://doi.org/10.1051/matecconf/202337904003

27. Yuan, Z.-G., Wang, Y.-X., Liu, Y.-Z., Wang, D., Jiao, W.-Z., andLiang, P.-F., Chinese J. Chem. Eng. **49** (2021) 178–186. doi: 10.1016/j.cjche.2021.12.023.
28. Chen, Y. S., Lin, F. Y., Lin, C. C., Der Tai, C. Y., and Liu, H. S., Ind. Eng. Chem. Res. **45** (2006) 6846–6853. doi: 10.1021/ie060399l.

Malaysian Journal of Catalysis 7 (2023) 49-53

Malaysian Journal of Catalysis
http://mjcat.utm.my/

MJCat
Research Article

Luffa Cylindrica Fibers Unveiled: A Sustainable Approach for 4-Nitrophenol Removal in Aqueous Solutions through Activated Carbon Utilization

Nurfatehah Wahyuny Che Jusoh[1,2]*, Nurhanani Mohd Azani[1], Nawal Abd Ghafar[1] and Khairunnisa Mohd Paad[1]

[1] *Department of Chemical and Environmental Engineering (ChEE), Malaysia-Japan International Institute of Technology (MJIIT), Universiti Teknologi Malaysia Kuala Lumpur, Jalan Sultan Yahya Petra, 54100 Kuala Lumpur, Malaysia.*
[2] *Center of Hydrogen Energy, Universiti Teknologi Malaysia Kuala Lumpur, Jalan Sultan Yahya Petra, 54100, Kuala Lumpur, Malaysia.*

**Corresponding Author: nurfatehah@utm.my*

Article history:
Received 4 November 2023
Accepted 24 December 2023

GRAPHICAL ABSTRACT

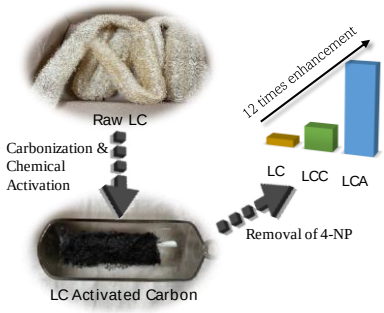

ABSTRACT

The prevalence of mutagenic and highly toxic compounds, such as 4-Nitrophenol (4-NP) and its derivatives, in industrial wastewater poses a significant environmental threat. This study emphasizes the critical need for public authorities to prioritize combating organic compound pollution for sustainable development. The focus of this research is the preparation and evaluation of activated carbon adsorbents derived from *Luffa cylindrica* fibers (LC) for the efficient removal of 4-NP from aqueous solutions. The preparation involved the carbonization process by heating LC in an argon furnace at 800 °C, resulting in carbonized *Luffa cylindrica* fibers (LCC). Subsequently, chemical activation is performed using a potassium hydroxide (KOH) solution, denoted as LCA. The properties of the adsorbent are identified through X-ray diffraction (XRD). To assess the removal efficiency of 4-NP, various parameters, such as pH, adsorbent dosage, and 4-NP solution concentration, are investigated. Optimal conditions for maximum 4-NP removal are achieved at a concentration of 50 mg/L, an adsorbent dosage of 0.75 mg/L (LCA), and a solution pH of 5. These conditions result in an impressive 99.9% removal of 4-NP in 60 minutes. This study demonstrates the feasibility of utilizing locally available raw materials, such as LC fibers, to prepare an adsorbent with a robust adsorptive capacity for toxic pollutants like 4-NP. The findings underscore the potential of eco-friendly solutions for addressing environmental challenges and promoting sustainable practices in wastewater treatment.

Keywords: *Luffa Cylindrica, 4-Nitrophenol, Activated Carbon, Sustainable, Wastewater*

| eISSN 0128-2581 |

1. INTRODUCTION

The persistent challenge of various organic and inorganic constituents present in industrial effluents, particularly in Malaysia's surface and wastewater, remains a longstanding environmental concern. Phenol, known for its high solubility in water, oils, carbon disulfides, and various organic solvents, is a significant contributor to this issue [1]. Originating from both natural and chemical processes associated with industrial or human activities, the introduction of phenol and phenolic compounds into water poses a significant threat to the environment and ecosystems. Phenol, a crucial organic synthetic raw material, finds widespread application in the production of dyes, plasticizers, pharmaceuticals, and antioxidants [2].

One such phenolic compound, 4-Nitrophenol (4-NP), characterized by functional groups NN and OH on the benzene ring, is well-known for its presence in industrial effluents, contributing to unpleasant odors and tastes that can lead to carcinogenic problems. Acute exposure to 4-NP has been linked to various health issues, including blood disorders, kidney and liver damage, skin and eye irritation, anemia, and systemic poisoning in humans [3]. Consequently, governments have enacted laws to monitor and control 4-NP levels in both drinking water and effluents discharged from factories.

Several techniques have been developed to address the removal of 4-NP from contaminated water, such as adsorption, chemical oxidation, electrocoagulation, solvent extraction, and membrane separation. Among these, the adsorption process stands out for its efficiency in removing certain organic matter from waste effluents, boasting advantages such as initial cost-effectiveness, flexibility, and ease of operation. Activated carbons, renowned for their exceptional adsorption capabilities for organic pollutants, have been widely utilized, although their high initial cost and

the need for a costly regeneration system pose economic challenges. Consequently, researchers have explored low-cost, readily available alternatives, turning their attention to agricultural waste or industrial by-products as potential adsorbents.

For instance, Lv et al (2020) reported the preparation of activated carbon using rice husk via pyrolysis and potassium hydroxide (KOH)-activation. The rice husk-activated carbon possesses a high adsorption capacity for the removal of phenol. (325.27 mg/g) [4]. Additionally, Liu et al (2020) produce corn cob-activated carbon with have ability to remove 97.2% of mercury, Hg (II) in 120 min [5]. This shift is attributed to the economic and practical viability of adsorption by agricultural by-products, demonstrated in the removal of various pollutants, including phenol derivatives.

In this context, Luffa cylindrica fibers (LC), primarily composed of cellulose, hemicelluloses, and lignin in a proportion of 60%, 30%, and 10% by weight, respectively, emerge as a promising alternative adsorbent for the removal of 4-NP from aqueous solutions [6].

2. EXPERIMENTS

2.1 Preparation of *Luffa cylindrica* (LC) fibers, carbonized LC (LCC) and activated LC (LCA)

Luffa cylindrica fibers (LC) were obtained from a local market in Petaling Jaya, Malaysia. LC was cut into smaller pieces and washed multiple times to remove any adhering dirt and seeds with deionized water. Next, LC was dried in an oven under 100 ℃ for 12 hours. After that, the LC was flattened using a cold-press machine and placed in a sample boat to undergo the carbonization process in a furnace under an argon atmosphere. The LC was heated at a rate of 10 ℃/min and carbonized at 800 ℃ for 1 hour. The obtained sample was denoted as LCC.

Then the LCC was activated using potassium hydroxide (KOH) by mixing in a mass ratio of 1:2 in 30 mL of deionized water for 10 hours, then dried in an oven at 80 ℃. The mixture was heated again in an argon furnace at 700 ℃ at a rate of 10 ℃/min for 1 hour. Then, it was washed thoroughly with 1 M hydrochloric acid (HCl) to remove any inorganic salts. The sample will be washed a second time with deionized water to remove the acid and dried in an oven at 80 ℃ overnight. Thus, the activated sample was denoted as LCA.

2.2 Characterization

The structures of the adsorbent were determined by the X-ray diffraction (XRD) method with Cu-kα radiation, λ = 1.54 Å as an X-ray source at 25°C using the Empyrean Multi-Purpose Research X-Ray Diffractometer. The accelerating voltage was 40 kV, and the applying current was 40 mA.

2.3 Removal of 4-Nitrophenol (4-NP)

Adsorbent activity was evaluated in the adsorption of 4-Nitrophenol (4-NP) through a series of batch experiments. Various concentrations of 4-NP solution (ranging from 10 to 100 mg/L) were stirred (200 rpm) at room temperature, ensuring even dispersion of the adsorbent (dosages between 0.25 to 1.00 g/L). The pH of the solution was adjusted to the desired level using 0.1 M HCl or 0.1 M NaOH. At predetermined intervals, 3 ml aliquots were withdrawn, centrifuged, and then analysed using a UV-Vis spectrophotometer (Shimadzu UV-2600i, Japan) at 318 nm and 400 nm for acidic and basic samples, respectively, to determine the remaining concentration of 4-NP. Each experimental set was conducted in triplicate, and the removal percentage was calculated using the formula provided,

$$Removal\ [\%] = \frac{C_0 - C_t}{C_0} \times 100$$

where C_0 and C_t represent the initial and time-dependent concentrations of 4-NP, respectively.

3. RESULTS AND DISCUSSION

3.1 Characterization

The XRD analysis was conducted on LC, LCC, and LCA adsorbents. Figure 1 illustrates the XRD patterns obtained for each of these samples.

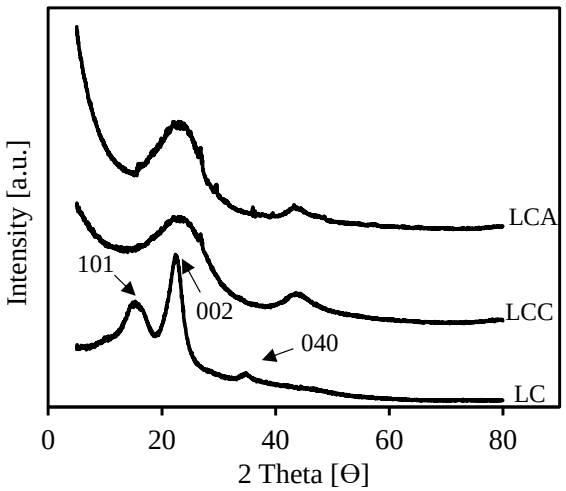

Figure 1. XRD pattern of LC, LCC and LCA adsorbents

The XRD pattern of LC displays characteristic features synonymous with cellulose, featuring well-defined diffraction signals at 2θ=15.4°, 22.5°, and 34.2°, corresponding to specific crystallographic planes, namely (101), (002), and (040), respectively [7]. Notably, two relatively broad diffraction peaks are observed around 23° and 44°, indicating the amorphous nature of both LCC and LCA samples.

Furthermore, the XRD analysis reveals distinctions between LCA and LCC. LCA exhibits a relatively intense peak compared to LCC, suggesting an increased degree of graphitization in the sample following the activation process. This enhanced graphitization signifies structural changes and modifications in the activated carbon, highlighting the impact of the activation process on the crystalline properties of the adsorbent [8].

3.2 Adsorption Study

The adsorption study encompassed a comprehensive exploration of the impacts of different factors, including the type of adsorbents, pH variations, adsorbent dosage, and 4-NP concentration. Within the effect of adsorbents, a comparative analysis was conducted among the three distinct adsorbents—LC, LCC, and LCA. The results, as depicted in Figure 2, revealed a distinctive adsorption behavior characterized by an initial rapid adsorption phase within the first 3 mins, followed by a slower adsorption phase that persisted until reaching a plateau at approximately 60 mins.

It is noteworthy that LC exhibited the lowest removal efficiency for 4-NP (8%). However, the carbonization process resulted in a notable improvement in adsorption properties, as evidenced by LCC, which exhibited a considerable increase to 25%. The subsequent activation process further enhanced the graphitization of the absorbent in LCA, leading to a remarkable 12-fold increment in 4-NP removal, a significant improvement compared to the initial LC adsorbent performance (95%).

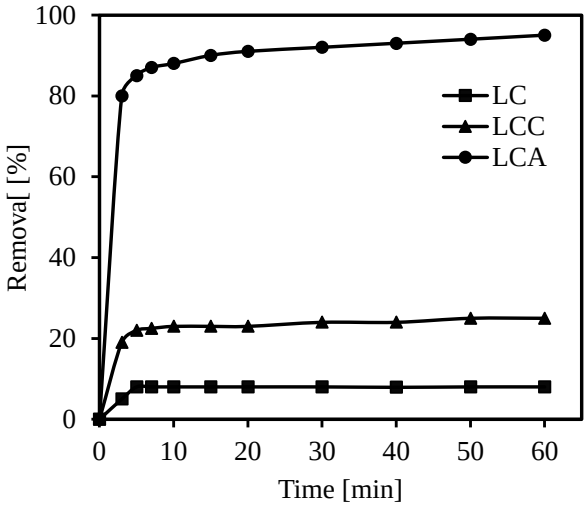

Figure 2. Effect of adsorbents (LC, LCC and LCA adsorbent) on removal of 4-NP [pH=5, adsorbent dosage=0.50 g/L, initial 4-NP concentration=50 mg/L, time=60min]

These results point out the significance of carbonization and activation steps in an argon atmosphere. The strength of adsorption is thought to be improved in the presence of argon, which promotes a greater internal porosity and higher effective surface area than raw LC [9, 10]. This has considerable value for specialized absorbents in practical applications to remove pollutant entities from solution or atmospheres. [9].

The subsequent parameter investigated in the adsorption study was the impact of solution pH on the removal of 4-NP using the LCA adsorbent. Solution pH plays a pivotal role in adsorption studies, as it has the potential to influence the surface charge of the adsorbent, as highlighted in previous research [11]. For this investigation, solution pH levels of 3, 5, 8, and 11 were selected. Figure 3 illustrates that the removal efficiency of 4-NP reached its maximum and remained relatively unaffected when the initial pH of the solution was within the range of 3 to 5. However, a noticeable decrease occurred as the pH of the solution increased beyond this range. This finding suggests that the adsorption of 4-NP is more pronounced in acidic solutions compared to basic solutions, and the percentage adsorption of 4-NP diminishes with an increase in the alkalinity of the medium [9]. This insight into the pH effect on adsorption is crucial for optimizing the conditions for the efficient removal of 4-NP in practical applications.

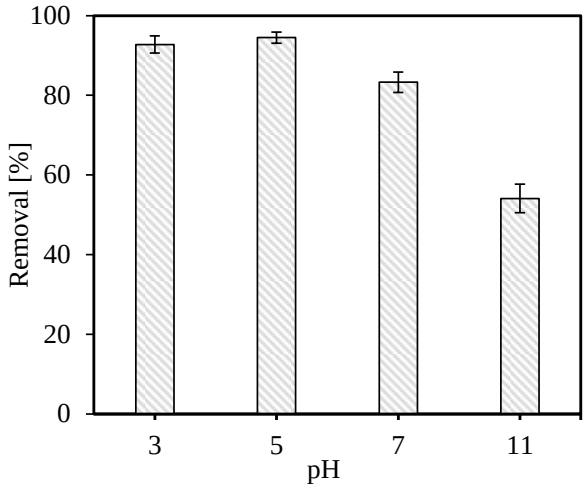

Figure 3. Effect of pH on 4-NP adsorption onto LCA adsorbent [Adsorbent dosage=0.50 g/L, initial 4-NP concentration=30 mg/L, time=60min]

Then, the influence of adsorbent dosage on the adsorption of 4-NP using the LCA adsorbent was investigated. Adsorbent dosage plays a critical role in adsorption studies, serving as the source of active sites for the adsorption of the dye molecules. The process temperature range explored in this study ranged from 0.25 to 1.0 g/L. The graphical representation of the effect of adsorbent dosage on 4-NP adsorption using the LC-A adsorbent is depicted in Figure 4. Notably, the percentage of 4-NP removal exhibited a discernible increase with the rising adsorbent dosage, ranging from 0.25 to 0.75 g/L, resulting in a removal efficiency increase from 89% to 98.5%.

This observed trend can be attributed to the escalating number of sorption sites available at the adsorbent surface as the adsorbent dosage increases, thereby enhancing the percentage of 4-NP removal from the solution [12, 13]. However, it is noteworthy that further increases in adsorption dosage, up to 100 mg, did not yield a significant increment in removal efficiency, stabilizing at 99%. Therefore, 75 mg of adsorbent dosage was deemed optimal for the subsequent investigation into the adsorption of 4-NP at varying concentrations.

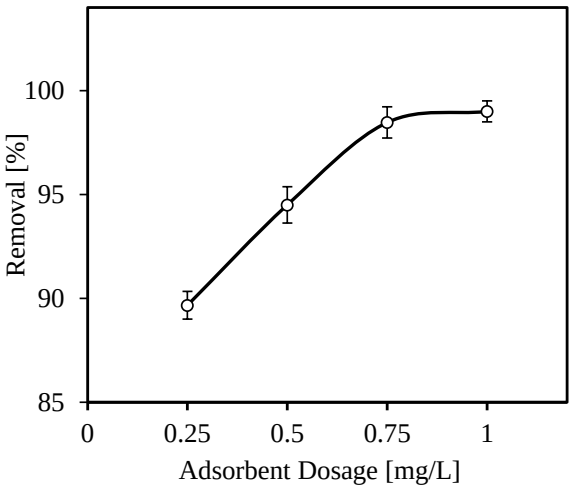

Figure 4. Effect of adsorbent dosage on 4-NP adsorption onto LCA adsorbent [pH=5, and initial 4-NP concentration=30 mg/L, time=60min]

Finally, the impact of the initial 4-NP concentration on the adsorption using the LCA adsorbent was investigated, focusing on a range of initial 4-NP concentrations from 10 to 100 mg/L. The graphical representation of this study is illustrated in Figure 5. Observations from the figure indicate a slight increase in the removal of 4-NP as the initial concentration rises from 10 mg/L to 50 mg/L, resulting in removal efficiencies of 95%, 98%, and 99% for 10 mg/L, 30 mg/L, and 50 mg/L, respectively.

However, further increases in the initial 4-NP concentration, up to 100 mg/L, led to a reduction in removal efficiency from 99% to 94.6%. This decline in removal efficiency with an increase in initial 4-NP concentration can be attributed to the potential saturation of adsorption sites on the LCA adsorbent. As the concentration of 4-NP in the solution rises, the available adsorption sites become saturated, leaving unadsorbed 4-NP in the aqueous solution [14]. These insights are crucial for understanding the behaviour of the adsorption system and for finding the best conditions for practical applications.

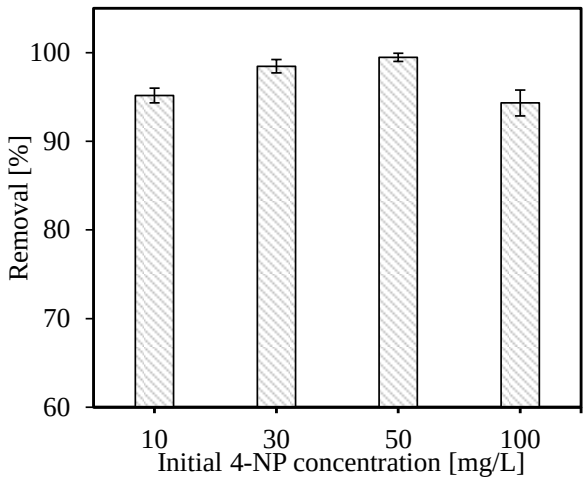

Figure 5. Effect of 4-NP initial concentration on adsorption onto LCA adsorbent [pH=5, and 0.75 mg of adsorbent dosage; time: 60 min]

4. CONCLUSION

This study successfully produced *Luffa cylindrica* fibers (LC) activated carbon adsorbent through carbonization and chemical activation with potassium hydroxide (KOH). The LC activated carbon (LCA) demonstrated remarkable properties, achieving a 99% removal efficiency for 4-NP under optimized conditions (pH=5, adsorbent dosage=75 mg, and initial 4-NP concentration of 50 mg/L). Notably, LCA outperformed LCC and LC, attributed to its chemical activation and heightened adsorption capabilities. The utilization of locally sourced raw materials, like *Luffa cylindrica* fibers, proved effective in creating a highly porous adsorbent with a significant 4-NP removal capacity. This approach, employing low-cost adsorbent, holds promise for environmental sustainability, potentially replacing commercial activated carbon in certain applications and emphasizing the importance of resourceful solutions for environmental challenges.

ACKNOWLEDGEMENTS

This work was supported by the Ministry of Higher Education Malaysia under Fundamental Research Grant Scheme, UTM, FRGS/1/2022/STG05/UTM/02/2.

REFERENCES

1. Al-Ananzeh, N., et al., Results in Engineering. **20** (2023) 101404.
2. Yin, H., et al., Microchimica Acta. **169** (2010) 87-92.
3. Serrà, A., et al., Catalysts. **10** (2020) 458.
4. Lv, S., et al., Applied Surface Science. **510** (2020) 145425.

5. Liu, Z., et al., Bioresource Technology. **306** (2020) 123154.
6. Frollini, E., et al., Natural Polymers and Agrofibers Composites. (2000).
7. Nadaroglu, H., S. Cicek, and A.A. Gungor, Spectrochimica Acta - Part A: Molecular and Biomolecular Spectroscopy. **172** (2017) 2-8.
8. Li, Z., et al., Colloids and Surfaces A: Physicochemical and Engineering Aspects. **538** (2018) 28-35.
9. Harimisa, G.E., et al., Chemical Engineering Research and Design. **198** (2023) 325-339.
10. Aghel, B., S. Behaein, and F. Alobaid, Fuel. **328** (2022) 125276.
11. Zhao, R., et al., Colloids and Surfaces A: Physicochemical and Engineering Aspects. **611** (2021) 125866.
12. Saber, S.E.M., et al., Radiation Physics and Chemistry. **209** (2023) 110967.
13. Nitayaphat, W. and T. Jintakosol, Journal of Natural Fibers. **19** (2022) 3365-3377.
14. Ezzuldin M. Saber, S., et al., RSC Advances. **11** (2021) 8150-8162.

Malaysian Journal of Catalysis
http://mjcat.utm.my/
MJCat
Research Article

Effect of Transition Metal/Graphitic Carbon Nitride for Photoreduction of Hexavalent Chromium

M.S. Azami[1, *], A.R. Faatihah[1], A.H. Nordin[1], K.H. Tan[2], N. Jamaluddin[3], N.M. Izzudin[4], A.A. Azmi[5]

[1] *Faculty of Applied Sciences, Universiti Teknologi MARA, 02600 Shah Arau, Perlis, Malaysia*
[2] *Centre for Advanced Materials, Faculty of Engineering and Technology, Tunku Abdul Rahman University of Management and Technology, 53300 Kuala Lumpur, Malaysia*
[3] *Faculty of Science, Universiti Teknologi Malaysia, 81310 UTM Johor Bahru, Johor, Malaysia*
[4] *School of Chemical and Energy Engineering, Faculty of Engineering, Universiti Teknologi Malaysia, 81310 UTM Johor Bahru, Johor, Malaysia.*
[5] *Graduate School of Science and Engineering, Saga University, 1 Chome Honjomachi, Saga, 840-8502, Jepun*

**Corresponding Author: saifulddin@uitm.edu.my*

Article history:
Received 13 November 2023
Accepted 27 December 2023

ABSTRACT

Recently, the discharge of heavy metals such as hexavalent chromium (Cr (VI)) into water is increasing due to the development of industrials. This poses a huge environmental challenges as toxic waste of heavy metal leads to water pollution which give a negative impact on health and environment. This heavy metal can be treated by reducing the highly poisonous of Cr (VI) to less toxic trivalent chromium Cr (III). Nowadays, the photocatalytic reduction is one of the effective methods that can reduce Cr (VI) to harmless toxic into the environment. In this study, the effect of different metal of Ag, Cu and Ni loaded on g-C_3N_4 were investigated based on the structural, morphological, compositional, and optical properties. The different metal of Ag, Cu and Ni were loaded on g-C_3N_4 by using impregnation method. The physical and chemical properties of Ag, Cu and Ni loaded on g-C_3N_4 were analyzed using FTIR and UV-vis/DRS techniques. The performance of photocatalytic activity among Ag, Cu and Ni loaded on g-C_3N_4 were evaluated for photoreduction of Cr (VI) and the highest performance of photoreduction of Cr (VI) was demonstrated by Ag/C_3N_4 (87%), followed by Cu/C_3N_4 (85%), Ni/C_3N_4 (80%) and pure g-C_3N_4 (77%) under visible-light. Among of photocatalyst, Ag/C_3N_4 was revealed as the best performance in photoreduction of Cr (VI) owing to its change in morphology, strong interaction between Ag and C N bonds and low band gap. Besides, the effect of scavengers shows the active species was the photogenerated electron (e^-) play an important role on photoreduction of Cr (VI). Overall, the Ag loaded on g-C_3N_4 was successfully contribute on photoreduction of Cr (VI) under visible light.

Keywords: *Hexavalent chromium, Transition metal, Graphitic carbon nitride, Photocatalyst, Impregnation method*

| eISSN 0128-2581 |

1. INTRODUCTION

The exposure of the Cr (VI) can cause high detrimental to human body including asthma, eye irritation and damage, perforated eardrums, respiratory irritation, kidney damage, liver damage, pulmonary congestion and edema, upper abdominal pain, nose irritation and damage, respiratory cancer, skin irritation, and erosion and discoloration of the teeth [1]. Therefore, many efforts have been done to reduce the Cr (VI) into Cr (III) by using electrocoagulation, biosorption, ion exchange, adsorption, and electrochemical reduction [2,3]. Unfortunately, these methods have several drawbacks such as costly in setup the treatment reactor, consuming a lot of time in treatment process, potential to produce secondary product and sewage sludge production [4].

The alternative approach to reduce Cr (VI) is by using photocatalytic reduction method due to its low cost, easy operation, and excellent safety [5]. By doing so, the extremely toxic Cr (VI) can be reduced to less toxic Cr (III) which is a trace element need by humans and easily precipitated in aqueous medium [5]. Graphitic carbon nitride (g-C_3N_4) is good potential photocatalyst for environmental remediation. The g-C_3N_4 is a non-metal-based semiconductor photocatalyst that has been extensively explored because of its non-toxicity, inexpensive cost, visible-light driven, narrow band gap, and great stability [6]. Furthermore, when compare to reduction potential of Cr (VI) to Cr (III), the conduction band of g-C_3N_4 is more negative,

indicated that the photo-generated electrons of g-C_3N_4 have a high thermodynamic driving force to cause a reduction of Cr (VI) into Cr (III) [7]. However, there are some disadvantages of using g-C_3N_4 such as low utilization rate of visible-light, rapid recombination of electron hole pairs, and small specific surface area [8]. In recent research, transition metal has been shown a good potential to overcome these issues and therefore, enhance the photocatalytic activity of g-C_3N_4. This is because, the presence of transition metals inhibited the recombination of electron-hole and enhanced the visible light absorption [9]. Therefore, it is an effective strategy to improve the application of g-C_3N_4 under visible light as it modifies the structure of the electronic band gap by metal doping [10].

In this study, the different transition metals such as Ag, Cu and Ni have been chosen to be loaded on g-C_3N_4 to enhance the photoreduction of Cr (VI). The presence of metal on g-C_3N_4 could formed new energy levels, extended the visible light response, and suppressed the electron-hole charge recombination rate [11]. Then, physical, and chemical properties of Ag, Cu and Ni loaded on g-C_3N_4 were investigated using FTIR and UV-vis/DRS in order to identify the functional group and optical properties of the prepared photocatalysts, respectively which can be correlated with the photocatalytic performance of photoreduction Cr (VI).

2. EXPERIMENTS

2.1 Preparation of g-C_3N_4

The g-C_3N_4 was synthesized by using urea under heat treatment method. 10 g of urea was placed into an alumina crucible and was covered with lid. Then the sample was calcined at 550 °C for 3 hours in air (5 °C/min) to obtained yellow colour of g-C_3N_4.

2.2 Preparation of Transition Metals Loaded on g-C_3N_4

The Ag, Cu and Ni loaded on g-C_3N_4 were prepared by using impregnation method. Firstly, 0.1 g of g-C_3N_4 was added into 25 mL of H_2O and stirred for 10 minutes. Then, 0.5 wt.% of $AgNO_3$ dissolved in 25 mL of H_2O was mixed into the g-C_3N_4 solutions. After that, the solution was stirred for 30 minutes at 50 ^oC and continuously stirred until dried at 80 ^oC. Next, the mixture was further dried in an oven at 100 °C for 3 hours. Finally, the sample was calcined at 550 °C for 3 hours and denoted as Ag/ g-C_3N_4. A similar procedure was repeated by using others metal precursor (Copper (II) Nitrate Trihydrate and Nickel (II) Sulfate Hexahydrate) loaded on g-C_3N_4, which denoted as Cu/g-C_3N_4 and Ni/g-C_3N_4 respectively.

2.3 Characterization of The Prepared Photocatalysts

The chemical composition analysis was examined using Fourier transform infrared (FTIR) via KBR method (Agilent with model instrument Cary 640), The absorbance of optical properties for the prepared photocatalysts was determined using (Agilent Cary 60) ultraviolet-visible/diffuse reflectance spectra (UV-Vis/DRS) spectrophotometer.

2.4 Photocatalytic Reduction of Cr (VI)

The photocatalytic activity of Ag/C_3N_4, Cu/C_3N_4 and Ni/C_3N_4 photocatalyts were investigated for reduction of Cr(VI) under visible light. The 300 W xenon lamp was used as radiant source. The prepared photocatalyst was added (0.0094 g) to the mixture of 25 mL of $K_2Cr_2O_7$, 1 mL of diphenylcarbazide solution (indicator) and a drop of of H_2SO_4. The concentration of Cr(VI) was measured using 1,5-diphenylcarbazide (DPC) method which the sample's absorbance was measured at 540 nm by carried out using UV-Vis spectrophotometer. The solution was stirred for 15 minutes in the absence of a light source to achieve adsorption-desorption equilibrium between the catalyst and Cr (VI) and to determine the adsorption equilibrium time. After 15 min in the dark, the lamp was turned on to start the photocatalytic reaction. Then, 3.0 mL of sample of Cr (VI) solution was collected and centrifuged for 15 minutes.

3. RESULTS AND DISCUSSION

3.1 Characterization of Photocatalyst

The optical properties for prepared photocatalysts were determined by UV/Vis DRS as depicted in Figure 1. Figure 1 (a) shows the UV–vis DRS analysis of the pure g-C_3N_4, Ag/C_3N_4, Cu/C_3N_4, and Ni/C_3N_4 at range of 200-800 nm. Figure 1 (b) shows the bandgap energy of each photocatalyst which converted from Kubelka-Munk equation. Based on the result, the steeper curve of Ag/C_3N_4 shows large absorption band in the visible light region compared to pure g-C_3N_4. The optical band edge of g-C_3N_4 was observed at 480 nm. The absorbance of Ag/C_3N_4 extended further in the visible range of g-C_3N_4 is extrapolated at 500 nm. The shift of Ag/C_3N_4 indicate a potential of strong interaction between the C, N and Ag bonds that improve the efficiency of charge separation which enhance the activity of photoreduction [12]. Thus, Ag/C_3N_4 form more electron-hole pairs and absorb more photons can also give a significant performance on photoreduction of Cr (VI). Furthermore, the bandgap energy of g-C_3N_4, Ag/C_3N_4, Cu/C_3N_4 and Ni/C_3N_4 were determined to be 2.70, 2.60, 2.65 and 2.68 eV, respectively. Ag/C_3N_4 shows the lowest bandgap energy followed by Cu/C_3N_4, Ni/C_3N_4 and pure g-C_3N_4. The doped metal especially Ag/C_3N_4 shows the improvement in visible light absorption, decrease the recombination rate of electron-hole pairs as its reduce in the bandgap energy [13].

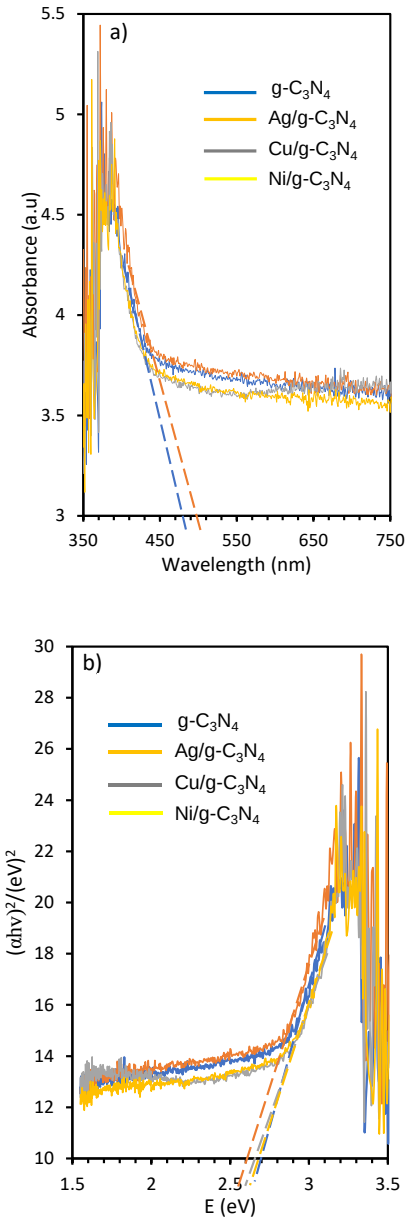

Figure 1. (a) UV-vis diffuse reflectance spectra (b) Plot of transformed Kubelka-Munk function versus energy of light for the prepared photocatalysts

The FTIR analysis was carried out to determine the funtional groups present in g-C_3N_4, Ag/C_3N_4, Cu/C_3N_4 and Ni/C_3N_4 with the range of 400-4000 cm^{-1} as shown in Figure 2. In the pure g-C_3N_4 photocatalyst (Figure 2 (d)), the vibrational broad peak shows at 3176.46 cm^{-1} indicate the present of N-H bond stretching associated with uncondensed amino groups and surface adsorbed water molecules [13]. The peaks at 1549.04 cm^{-1} to 1622.09 cm^{-1} corresponds to stretching mode of the C=N bond [14]. Meanwhile, the strong peaks observed in the region 1403.32 cm^{-1} can be attributed to the presence of aromatic of C-N heterocycles [15]. Then, the peak at 1234.19 cm^{-1} can be assigned to stretching vibrations of C–N–C or bridging C–NH–C bonds. The sharp peak at 806.11 cm^{-1} can be assigned to the s-triazine (heptazine) ring vibrations [16]. These peak indicate the synthesized of g-C_3N_4 is composed of heptazine units.

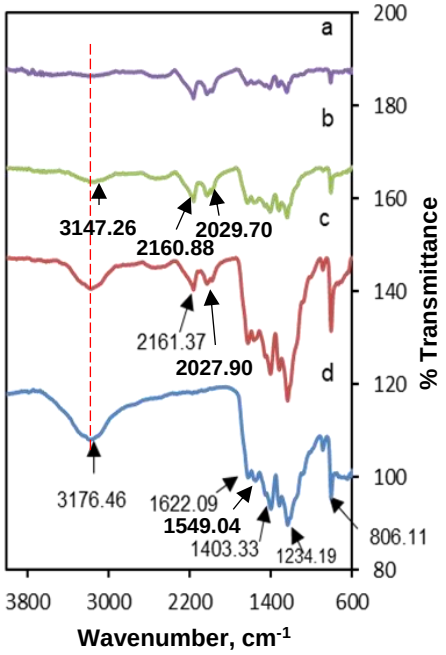

Figure 2. FTIR spectra of synthesized (a) Ni/C_3N_4, (b) Cu/C_3N_4, (c) Ag/C_3N_4 and (d) g-C_3N_4

Based on the FTIR, all the characteristic of vibrational peaks related to g-C_3N_4 can be observed in Ag/C_3N_4 photocatalyst (Figure 2(c)). This result showed that after modification of photocatalyts the structure of g-C_3N_4 is remained unchanged. However, the absorption peaks of N-H bonds gradually decrease with the additional of of Ag doping.This is because of Ag^+ can be anchored to amino groups through complexation and redox, then being photo-reduced to Ag^0 during photo-deposition process [17]. As a result, Ag nanoparticles form around the amino groups and interfere the stretching vibration of N-H bonds. Next, a peak at 2027.90 cm^{-1} and 2161.37 cm^{-1} is clearly observed in the Ag/C_3N_4 spectra but not in g-C_3N_4. This peak is attributed to the Ag-N stretching mode, indicating that silver atoms were successfully doped into the g-C_3N_4 crystal lattice [17]. Meanwhile, the stretching vibration frequencies of Cu/C_3N_4 differ slightly from pure g-C_3N_4 as can be seen in Figure 2 (b). The main absorption peak of N-H in the Cu/C_3N_4 composite at 3147.26 cm-1, indicating that there is not much shifted in the absorption peak position. However, it indicates that copper was successfully loaded onto g-C_3N_4, although the characteristics did not change much since Cu-N stretching mode appear at 2029.70 and 2160.85 cm^{-1} [18]. Meanwhile, Ni/C_3N_4 also shows slightly different from the pure g-C_3N_4. The main characteristic peak of the C=N (1575.60 and 1637.4 cm^{-1}) and C–N (1320.1 and 1410.95 cm^{-1}) stretching vibration frequency of the metal doped g-C_3N_4 was higher than the pure g-C_3N_4 as shown in Figure

2(a). The shifting of the C=N and C–N stretching frequencies are due to coordination of metal ions with the nitrogen atom in the g-C_3N_4.

3.2 Photocatalytic Performance

The photocatalytic activity performance of Ag, Cu and Ni loaded on g-C_3N_4 catalysts on the photoreduction of Cr (VI) were conducted under the visible light irradiation (Figure 3). It is observed that Ag/C_3N_4 (87%) is the most effective photocatalyst on photoreduction of Cr (VI) followed by Cu/C_3N_4 (85%), Ni/C_3N_4 (80%) and pure g-C_3N_4 (77%). This indicates that the pure g-C_3N_4 photocatalyst doping with metal improved photocatalytic reduction of Cr (IV). The lowest performance by g-C_3N_4 could be attributed to high recombination of electron-hole pair [14]. Meanwhile, the improvement on photoreduction of Cr (VI) over Ag/C_3N_4 could be impacted due to the high interaction between Ag and g-C_3N_4 with lowest bandgap (2.60 eV) as compared with others prepared photocatalyst, which enhanced the absorption of visible light.

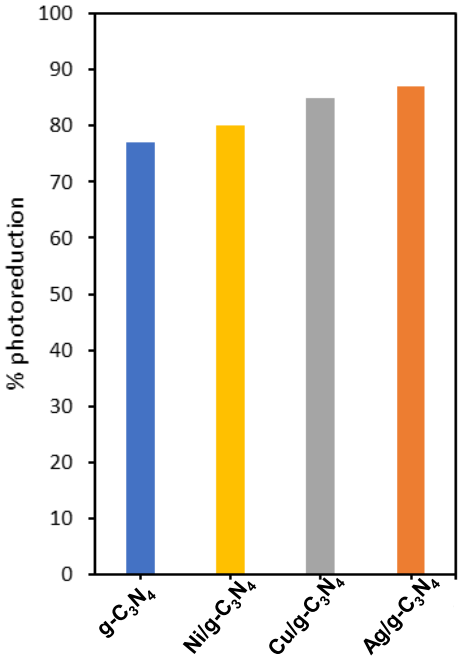

Figure 3. Photoreduction of Cr(VI) using pure g-C_3N_4, Ni/C_3N_4, Cu/C_3N_4 and Ag/C_3N_4 under visible light irradiation (($C_{Cr(VI)}$=10 mg L^{-1}, pH = 5, W = 0.375 g L^{-1}, t = 90 min)

3.3 Photoreduction Mechanism

The proposed mechanism for photoreduction of Cr (VI) was deduced by investigating the respective impact of photoactive radical species on the reaction. The effect of scavenger was performed to determine the role of scavenger species in the photocatalytic mechanism of Cr (VI) over Ag/C_3N_4. According to Figure 4, the photoreduction of Cr (VI) using Ag/C_3N_4 without scavenger species shows the best performance compared with the presence of scavenger. The experimental was examined by using Potassium Chlorate (PC) and Methanol (ME) as scavenger species for photogenerated electrons (e^-) and photogenerated holes (h^+) respectively. The scavengers determine that photogenerated e^- (70%) followed by photogenerated h^+ (72%) which shows slightly decrease in the performance of photoreduction of Cr (VI). Based on the result, the crucial active species was photogenerated e^- because of the lowest performance compared to h^+. Moreover, results indicate that the interaction of Ag on g-C_3N_4 show a significant contribution on photoreduction of Cr (VI) under visible light.

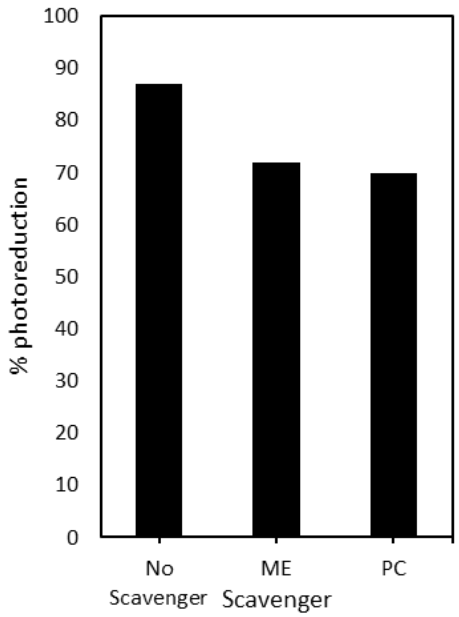

Figure 4. Photoreduction of Cr (VI) in the presence of scavenger using Ag/C_3N_4 photocatalyst ($C_{Cr(VI)}$=10 mg L^{-1}, pH = 5, W = 0.375 g L^{-1}, t = 90 min)

Figure 5 depicts the proposed of illustrated Ag/C_3N_4 mechanism. According to the effect of scavenger for Ag/C_3N_4, the photogenerated e^- and h^+ species shows favourable for the formation of a Schottky junction. The e^- was moved leaving h^+ from the valence band (VB) to the conduction band (CB) of g-C3N4. However, previous research reported the value of VB for g-C_3N_4 was about 1.23 eV. Noticeably illustrated that h^+ is incapable of converting H_2O to •OH because the potential level of •OH was 2.44 eV which higher compared to level of VB. Next, photogenerated e^- then move to Ag from CB of g-C_3N_4. The effectiveness of electromagnetic field may be improved by the Ag effect on the surface plasmonic resonance (SPR) because it potentially accelerates the rate of photogenerated electron-holes generation. As a result, the photogenerated e^- can react with O_2 to form $•O_2^-$. This species is in charge of increasing activity on photoreduction Cr (VI). Therefore, the mechanism described above show that the loading of Ag on g-C_3N_4 was generate a Schottky junction. Schottky junction

photocatalyst demonstrates how the interaction of Ag and g-C_3N_4 increased the electron generated and play as a catalyst for more effectively capturing light and transferring charge, hence increase the activity on photoreduction of Cr (VI).3.

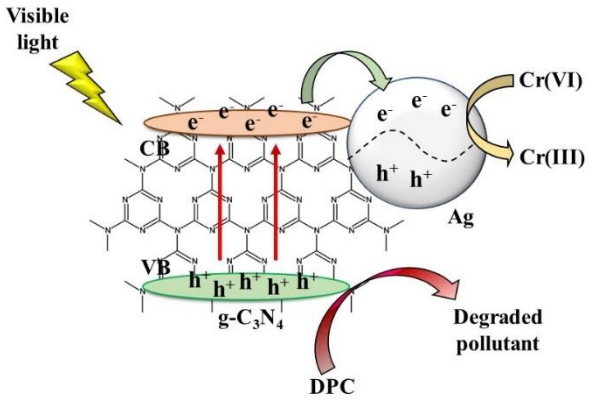

Figure 5. Mechanism of photocatalytic activity of Ag/C_3N_4.

4. CONCLUSION

g-C_3N_4 was prepared using urea as a precursor and loaded with metal using impregnation method to enhance the photoreduction activity. The physical and chemical properties of the photocatalysts were examined using, FTIR and UV-Vis DRS. The highest performance of photoreduction of Cr (VI) was demonstrated by Ag/C_3N_4 (87%), followed by Cu/C_3N_4 (85%), Ni/C_3N_4 (80%) and pure g-C_3N_4 (77%) under visible-light. Among of photocatalyst, Ag/C_3N_4 was revealed as the best performance in photoreduction of Cr (VI) due to strong interaction between Ag and C, N bonds and low band gap. Moreover, the effect of scavenger shows the active species was the photogenerated electron (e^-) play an important role on photoreduction of Cr (VI). Overall, the Ag loaded on g-C_3N_4 was successfully contribute on photoreduction of Cr (VI) under visible light.

ACKNOWLEDGEMENTS

The authors are grateful for the financial support by the Research University Grant from Universiti Teknologi MARA (Grant No. PY/2023/00444).

REFERENCES

1. Wu, J. H., Shao, F. Q., Han, S. Y., Bai, S., Feng, J. J., Li, Z., & Wang, A. J., Journal of Colloid and Interface Science. **535** (2019) 41–49. https://doi.org/10.1016/j.jcis.2018.09.080
2. Hasija, V., Raizada, P., Singh, P., Verma, N., Khan, A. A. P., Singh, A., Selvasembian, R., Kim, S. Y., Hussain, C. M., Nguyen, V. H., & Le, Q. Van. Process Safety and Environmental Protection, **152** (2021).663–678. https://doi.org/10.1016/j.psep.2021.06.042.
3. Liu, S., Zhang, W., Zhu, P., Zuo, S., & Xia, H. Journal of Environmental Chemical Engineering, (2021). https://doi.org/10.1016/j.jece.2021.105879.
4. Azami, M. S., Jalil, A. A., Aziz, F. F. A., Hassan, N. S., Mamat, C. R., Fauzi, A. A., & Izzudin, N. M., Separation and Purification Technology, 292 (2022) 120984. https://doi.org/10.1016/j.seppur.2022.120984.
5. Islam, J. B., Furukawa, M., Tateishi, I., Katsumata, H., & Kaneco, S., ChemEngineering, 3 (2019) 1–10. https://doi.org/10.3390/chemengineering302003.
6. Lin, H., Wu, J., Zhou, F., Zhao, X., Lu, P., Sun, G., Song, Y., Li, Y., Liu, X., & Dai, H., Journal of Environmental Sciences, **124** (2021) 570–590. https://doi.org/10.1016/j.jes.2021.11.017.
7. Barolo, G., Livraghi, S., Chiesa, M., Paganini, M.C., Giamello, E., Journal of Physical Chemistry. (2012) 20887-20894.
8. Orlando C-Neto and Maurício S. B., Cosmeticscope. **21** (2015) 4.
9. Prabakaran, E., & Pillay, K., ACS Omega, **6** (2021) 35221–35243. https://doi.org/10.1021/acsomega.1c00866
10. Viet, N. M., Trung, D. Q., Giang, B. L., Tri, N. L. M., Thao, P., Pham, T. H., Kamand, F. Z., & Al Tahtamouni, T. M., Journal of Water Process Engineering, **32** (2019) 100954. https://doi.org/10.1016/j.jwpe.2019.100954
11. Jiang, L., Yuan, X., Pan, Y., Liang, J., Zeng, G., Wu, Z., & Wang, H., Applied Catalysis B: Environmental, **217** (2017) 388–406. https://doi.org/10.1016/j.apcatb.2017.06.003
12. Yan, W., Yan, L., & Jing, C. Applied Catalysis B: Environmental, **244** (2019) 475–485. https://doi.org/10.1016/j.apcatb.2018.11.069
13. Zhang, Y., Yuan, J., Ding, Y., Liu, B., Zhao, L., & Zhang, S., Ceramics International, **47** (2021) 31005–31030. https://doi.org/10.1016/j.ceramint.2021.08.063
14. Azami, M. S., Jalil, A. A., Nawawi, W. I., Mamat, C. R., & Izzudin, N. M., Materials Today: Proceedings, **66** (2022) 4068–4072.
15. Durairaj, A., Sakthivel, T., Obadiah, A., & Vasanthkumar, S., Journal of Materials Science: Materials in Electronics, **29** (2018) 8201–8209. https://doi.org/10.1007/s10854-018-8826-5.
16. Faisal, M., Ismail, A. A., Harraz, F. A., Al-Sayari, S. A., El-Toni, A. M., & Al-Assiri, M. S. Materials and Design, **98** (2016) 223–230. https://doi.org/10.1016/j.matdes.2016.03.019
17. Hayat, A., Al-Sehemi, A. G., El-Nasser, K. S., Taha, T. A., Al-Ghamdi, A. A., Jawad Ali Shah Syed, Amin, M. A., Ali, T., Bashir, T., Palamanit, A., Khan, J., & Nawawi, W. I., International Journal of Hydrogen Energy, **47** (2022), 5142–5191.